

# Aluminum alloys and single crystals studied by XPEEM, XPS, and XRR

LISA RULLIK

DEPARTMENT OF PHYSICS | FACULTY OF SCIENCE | LUND UNIVERSITY



# Aluminum alloys and single crystals studied by XPEEM, XPS, and XRR

by Lisa Rullik



**LUND**  
UNIVERSITY

LICENTIATE THESIS

Thesis advisors: Prof. Edvin Lundgren, Prof. Anders Mikkelsen

Faculty opponent: Dr. Maria Messing

To be presented, with the permission of the Faculty of Science, Lund University, for public criticism in the lecture hall K457 at the Division of Synchrotron Radiation Research, Department of Physics on Friday the 16<sup>th</sup> of June 2017 at 10:15 am.

A Licentiate's degree at a university in Sweden is a recognised pre-doctoral degree, which is formally equivalent to half of a doctoral dissertation.

**Cover image:**

Dark field image of a polycrystalline aluminum sample taken with 10x magnification in an optical microscope.

**Funding information:** The thesis work was financially supported by Swedish Foundation for Strategic Research (SSF project RMA11-0090, Aluminum oxides for processing and products (ALUX)).

© Lisa Rullik and the respective publishers

Faculty of Science  
Department of Physics  
Division of Synchrotron Radiation Research

ISBN: 978-91-7753-335-1 (print)

ISBN: 978-91-7753-336-8 (pdf)

Printed in Sweden by Media-Tryck, Lund University, Lund 2017



SI HOC LEGERE SCIS NIMIUM ERUDITIONIS HABES



# Contents

<b>Preface</b>	<b>iii</b>
List of Publications . . . . .	iv
Abstract . . . . .	v
Populärwissenschaftliche Zusammenfassung . . . . .	vi
Populärvetenskaplig sammanfattning . . . . .	viii
Acknowledgements . . . . .	x
<b>Aluminum alloys and single crystals studied by XPEEM, XPS, and XRR</b>	<b>1</b>
1 Introduction . . . . .	2
2 Materials . . . . .	4
2.1 Pure Aluminum . . . . .	5
2.2 Aluminum Oxide . . . . .	7
2.3 Aluminum Alloys . . . . .	11
2.4 Brazing Sheets . . . . .	15
3 Instrumentation and Methods . . . . .	17
3.1 X-rays and Synchrotron Radiation . . . . .	17
3.2 X-ray Reflectivity . . . . .	18
3.3 Spectroscopy . . . . .	20
3.4 Microscopy . . . . .	23
4 Summary of Papers . . . . .	29
5 Outlook . . . . .	31
References . . . . .	32
<b>Scientific publications</b>	<b>39</b>
Paper I: The thickness of native oxides on aluminum alloys and single crystals . . . . .	41
Paper II: Surface development of an aluminum brazing sheet during heating studied by XPEEM and XPS . . . . .	51



# Preface

# List of Publications

This thesis is based on the publications listed below, which will be referred to as paper I and II. In both papers, I have contributed to the work. For paper II, I have been highly involved in planning and conducting the measurements, and I was main responsible for the analysis and the writing process.

I **The thickness of native oxides on aluminum alloys and single crystals**

J. Evertsson, F. Bertram, F. Zhang, L. Rullik, L.R. Merte, M. Shipilin, M. Soldemo, S. Ahmadi, N. Vinogradov, F. Carlà, J. Weissenrieder, M. Göthelid, J. Pan, A. Mikkelsen, J.-O. Nilsson, E. Lundgren  
Appl. Surf. Sci. 349 (2015) 826–832

II **Surface development of an aluminum brazing sheet during heating studied by XPEEM and XPS**

L. Rullik, F. Bertram, Y. R. Niu, J. Evertsson, T. Stenqvist, A. A. Zakharov, A. Mikkelsen, E. Lundgren  
Mater. Res. Express 3 (2016) 106506

All papers are reproduced with permission of their respective publishers.

Paper not included in this thesis, to which I have contributed:

III **Integration of electrochemical and synchrotron-based X-ray techniques for in-situ investigation of aluminum anodization**

F. Zhang, J. Evertsson, F. Bertram, L. Rullik, F. Carlà, M. Långberg, E. Lundgren, J. Pan  
Electrochim. Acta 241 (2017) 299–308

# Abstract

Aluminum is the most abundant metal in the earth's crust and it is nearly as abundant in our day-to-day life because of its characteristic properties: low weight, high tensile strength, and good corrosion and wear resistance due to a naturally occurring protective oxide layer. The aluminum products that we use in our daily life are however made of alloy aluminum instead of the pure metal since alloying a metal with other elements can lead to a better physical and mechanical performance. Even though metals like copper, tin, and zinc have been alloyed since approximately 2500 BC, modern research projects still try to unravel the interactions between the alloying elements on an atomic scale and their influence on various properties. Today's research efforts are characterized by attempts of moving from model systems and highly controlled and clean sample environments towards industrial standard alloys and *in-situ* experiments.

In this thesis we present results from measurements on single crystals, industrial aluminum alloy standards, and custom made composite aluminum alloys made for brazing applications. The thickness of the native aluminum oxide film covering three different single crystals and four industrial aluminum alloys was determined by X-ray reflectivity (XRR), X-ray photoelectron spectroscopy (XPS) as well as electrochemical impedance spectroscopy (EIS). These measurements were performed under a range of sample environments: ultra-high vacuum, vacuum, ambient, nitrogen, and liquid water conditions. It was shown that the native oxide thickness is dependent on the substrate and that alloys generally have a thicker oxide layer than single crystals. All three techniques depict this behaviour but the EIS gives smaller absolute values than the XRR and XPS measurements.

Further, XPS was used together with X-ray photoelectron emission microscopy (XPEEM) to follow the surface development of an aluminum brazing sheet during heating. The brazing sheet consists of a base alloy and an aluminum-silicon cladding, which is covered with a native aluminum oxide film. During heating to the melting temperature of the cladding changes in the chemical state of the alloying elements and their lateral distribution in the surface layer were detected. Magnesium was found to segregate to the surface upon heating, and the measurements indicate the formation of magnesium aluminate. Aluminum oxide as well as the silicon were observed to disappear from the surface during the heating.

# Populärwissenschaftliche Zusammenfassung

Aluminium ist das am häufigsten vorkommende Metall in der Erdkruste. In fast ähnlichem Umfang finden wir auch Aluminium in unserem Alltag, zum Beispiel in einer Espressokanne, einer Leiter oder einer Klimaanlage im Auto. Die hohe Verwendung ist aufgrund der charakteristischen Eigenschaften von Aluminium: geringes Gewicht, hohe Reißfestigkeit und gute Korrosionsbeständigkeit. Meistens wird jedoch nicht reines Aluminium als Werkstoff verwendet, sondern eine Aluminiumlegierung. Eine Legierung ist ein Gemisch aus mindestens einem Metall und einem weiteren Element. Diese Reinelemente werden in einer Schmelze miteinander verbunden. Daher wird auch das Verb *legieren*, hergeleitet aus dem lateinischen *ligāre*, was (zusammen)binden bedeutet, verwendet. Die Entwicklung von Legierungen sind von so außerordentlicher Bedeutung, dass sogar ganze Zeitalter danach benannt sind, wie die Bronzezeit nach der Legierung aus Kupfer und Zinn.

Typische Legierungselemente für Aluminium sind Silizium, Eisen, Kupfer, Mangan, Magnesium und Zink. Die unterschiedlichen Legierungen werden nach ihren Hauptlegierungselementen in verschiedene Gruppen eingeteilt. Die einzelnen Legierung in ihren Gruppen besitzen ähnliche physikalische und mechanische Eigenschaften. Desweiteren wird zwischen Knet- und Gusslegierungen unterschieden. Gusslegierungen finden unter anderem Anwendung im Fahrzeug- und Transportbereich, zum Beispiel als Felgen. In dieser Arbeit wurden unter anderem Knetlegierungen der 6XXX- und 7XXX-Gruppe studiert, da diese besonders korrosionsbeständig sind.

Für bestimmte Anwendungsgebiete ist es von Vorteil, mehrere Legierungen in einem sogenannten Verbundwerkstoff zu produzieren, da man die unterschiedlichen Eigenschaften der Legierungen nutzen möchte. In Hartlötblechen verwendet man den Unterschied der Schmelztemperaturen von zwei Legierungen, um Werkstoffe miteinander durch Hartlöten, Löten bei einer Temperatur von über 450°C, zu verbinden. Dabei schmilzt nur die Legierung an der Oberfläche, während die innere Legierung die Struktur erhält. Dieses Verfahren wird oft bei der Herstellung von Wärmewechslern in Autoklimaanlagen verwendet, da insbesondere in Lamellenwärmetauschern viele kurze Verbindungen zwischen den einzelnen Werkstoffen geschaffen werden müssen.

Bei der Korrosionsbeständigkeit von Knetlegierungen sowie beim Hartlöten von Verbundwerkstoffen aus Aluminium spielt die natürliche Oxidschicht eine bedeutende Rolle. In der vorliegenden Arbeit wurden daher Messmethoden aus der Oberflächenphysik angewendet. Die hier verwendeten Methoden haben gemein-

sam, dass sie Röntgenstrahlen zur Charakterisierung der Oberfläche nutzen. Die Röntgenstrahlen wurden dafür in einem kreisförmigen Teilchenbeschleuniger, einer sogenannten Strahlungsquelle, erzeugt. Synchrotronstrahlung wird hervorgerufen, wenn Elektronen, die in dem Beschleuniger Geschwindigkeiten nahe der des Lichtes haben, durch ein starkes Magnetfeld abgelenkt werden. Experimentelle Messstationen ermöglichen die Erforschung der Aluminiumproben mit den unterschiedlichsten Methoden, wie hier mit Röntgenreflektometrie, Röntgenphotoelektronenspektroskopie und Photoemissionselektronenmikroskopie. Diese Messmethoden geben Informationen über die Dicke der Oxidschicht, die Elemente in ihr und deren chemischer Zustand sowie deren laterale Verteilung.

Die Erforschung, wie sich diese Eigenschaften durch Einwirkung von verschiedenen Probenumgebungen verändern, ist ein Teil des ALUX- (ALUminium oXides for processing and products) Projektes, in dessen Rahmen die vorliegende Arbeit angefertigt wurde. Das Projekt hat sich zum Ziel gesetzt, mit neuen Messmethoden und grundlegenden Theorien zu der Entwicklung von Aluminiumprodukten mit verbesserter Vielseitigkeit und Korrosionsbeständigkeit beizutragen. Um dies zu erreichen, haben sich experimentelle und theoretische Physiker mit der schwedischen Aluminiumindustrie innerhalb des ALUX-Projektes zusammengeschlossen.

Meine Arbeit trägt zu diesem Ziel bei, indem sie klassische oberflächenphysikalische Methoden für die Charakterisierung von komplexen Aluminiumlegierungen und deren Oxidschichten verwendet. Dabei liegt ein besonderer Fokus auf Messungen in realistischen Probenumgebungen, im Gegensatz zu den klassischen Ultrahochvakuumexperimenten der Oberflächenphysik. Die bisherigen Experimente dieser Arbeit haben zu der Publikation von zwei wissenschaftlichen Artikeln beigetragen, die sich zum einen mit der Dicke und chemischen Zusammensetzung der Oxidschicht auf unterschiedlichen Substraten und in verschiedenen Probenumgebungen beschäftigt und zum anderen mit der Zersetzung der Aluminiumoxidschicht auf Hartlötblechen während des Erhitzens. Die Publikationen sind im zweiten Teil dieser Abhandlung zu finden.

# Populärvetenskaplig sammanfattning

Aluminium är den vanligaste metallen i jordskorpan och nästan lika vanlig i våra dagliga liv som i kaffebyggare, stegar, eller i luftkonditioneringen i bilar. Detta är på grund av aluminiums karaktäristiska egenskaper: låg vikt, hög hållfasthet och god korrosionsbeständighet. Emellertid används inte ren aluminium inom många tillämpningar utan istället används aluminiumlegeringar. En legering är en blandning av åtminstone en metall och ett annat grundämne. Den rena metallen sammanförs vanligtvis med de andra elementen i en smälta. Utvecklingen av legeringar är av utomordentligt betydelse för mänskligheten och även tidsepoker har benämnts efter dem, t.ex. bronsåldern efter legeringen av koppar och tenn.

Vanliga legeringsämnen till aluminium är kisel, järn, koppar, mangan, magnesium och zink. De olika legeringarna är indelade i grupper beroende på deras huvudsakliga legeringsämne. De olika legeringarna inom en grupp har liknande fysikaliska och mekaniska egenskaper. En ytterligare uppdelning finns mellan smidda och gjutna legeringar. Gjutna legeringar används bland annat i fordons- och transportsektorn, så som till fälgar. I det här arbetet studerades prover från 6XXX och 7XXX grupperna och några andra legeringar, vilka är särskilt resistenta mot korrosion.

För vissa tillämpningar är det av fördel att producera ett material av flera legeringar i ett så kallat kompositmaterial eftersom man vill använda de olika legeringarnas egenskaper. I hårdlodpläterade plåtar utnyttjar man skillnaden i smälttemperatur mellan de båda legeringarna i kompositmaterialen under hårdlödning. Att hårdlöda innebär att man sammanfogar material vid en temperatur över 450°C men lägre än smältpunkten av materialen som ska sammanfogas. Det betyder att endast legeringen på ytan smälter medan den inre legeringen uppehåller fast form. Denna metod används ofta vid framställning av värmeväxlarna i luftkonditioneringssystem eftersom man måste skapa många korta kopplingar mellan materialen i lamellära värmeväxlare.

Det naturliga oxidskiktet av aluminium spelar en viktig roll i korrosionsbeständigheten hos legeringarna samt i hårdlödning av kompositmaterial, därför användas ytfysikaliska mätmetoder i det här arbete. De metoder som används i denna avhandling har gemensamt att de använder röntgenstrålar för att karakterisera ytan. De röntgenstrålar som används genereras i en cyklisk partikelaccelerator som kallas synkrotron. Synkrotronstrålning uppstår när elektroner, som i acceleratoren har en fart nära ljusets, böjs genom ett starkt magnetfält. Experimentstationer tillåter forskning på aluminium prover med olika metoder, så som rönt-

genreflektion, röntgenfotoelektron-spektroskopi och fotoemissionselektronmikroskopi. Dessa mätmetoder ger information om tjockleken på oxidskiktet, elementen i oxidskiktet och deras kemiska tillstånd och rumsliga distribution.

Att studera hur dessa egenskaper förändras på grund av olika provmiljöer är en del av ALUX (ALUminium oXides for processing and products) projektet i vilket detta arbete utförts. Projektets mål är att använda nya mätmetoder och grundläggande teorier för att bidra till utveckling av aluminiumprodukter med förbättrad mångsidighet och korrosionsbeständighet. För att nå detta mål inleddes ett samarbete mellan experimentella och teoretiska fysiker och den svenska aluminiumindustrin i ett gemensamt projekt: ALUX projektet.

I detta arbete så har vi försökt att nå vissa delmål inom ALUX projektet, genom att tillämpa klassiska ytfysiska metoder för karakterisering av komplexa aluminiumlegeringar och deras oxidskikt. En särskild inriktning ligger på mätningar i realistiska provmiljöer i motsats till de klassiska experiment inom ytfysik som utförs i ultrahögvakuum. Hittills har mitt arbetet bidragit till publiceringen av två vetenskapliga artiklar: den första fokuserar på tjockleken och den kemiska sammansättningen av oxidskiktet på olika substrat och i olika provmiljöer, den andra på nedbrytningen av aluminiumoxidskiktet på hårdlodpläterade plåtar under upphettning. Publikationer finns i den andra delen av denna uppsats.

## Acknowledgements

First of all, I would like to thank my supervisor, Edvin Lundgren, for all his patience and his encouraging attitude to try out and learn something new. I am very thankful for his support and our discussion about science, research, teaching, and everything else.

I would also like to thank my co-supervisor, Anders Mikkelsen, for his help with writing my first paper and this thesis, especially when it comes to PEEM.

Further, I would like to thank Florian Bertram, Jonas Evertsson, and Nikolay Vinogradov for their help before, during, and after all the beamtimes we had together. When it comes to PEEM beamtimes I would like to thank Alexei Zakharov and Yuran Niu for their patience during the experiments and I would like to especially thank Alexei for his help with the data analysis. I would also like to thank Milad Yazdi and Mats Göthelid for the nice XPS beamtimes.

I would like to thank Torkel Stenqvist and Jan-Olov Nilsson for providing me with samples and an insight into the aluminum industry. With that I would also like to thank all members of the ALUX project for the lively discussions about my data.

Lively discussion also occur regularly in the divisions lunch room and therefore I would like to thank all of my colleges at SLJUS. I would also like to thank Milena Moreira for the numerous cakes and sweet fika breaks. Further, I would like to thank Patrik Wirgin, Anneli Nilsson Ahlm, and Anne Petersson Jungbeck for their administrative support.

Finally, I would like to thank my familiy for their indulgence and Niclas Johansson for discussing data analysis over breakfast and dinner plans during beamtimes. Thank you for always being there for me!

# Aluminum alloys and single crystals studied by XPEEM, XPS, and XRR

# 1 Introduction

Aluminum is the third most abundant element in the earth's crust. Despite its great abundance, aluminum was not recognized as an element until the Danish physicist and chemist Hans Christian Ørsted succeeded in producing minor amounts of metallic aluminum by reacting potassium amalgam with anhydrous aluminum chloride. Later, in 1827, the German chemist Friedrich Wöhler succeeded in preparing the first pure sample of aluminum powder by using potassium and aluminum chloride [1].

A possible reason for the late discovery of aluminum can be given by its chemical properties. Aluminum is very reactive and when exposed to air it is almost only found in its various forms of oxide and silicate compounds. The high oxygen affinity of aluminum is the reason for the occurrence of its surprisingly adherent passive oxide film which is the foundation for its well-known corrosion resistance. Already the native oxide film, which is about 5 nm thick, provides a good corrosion protection.

The growth of a thicker protective layers is realized through electrochemical oxidation, which is known as anodization. By increasing the thickness of the oxide layer the corrosion protection properties of the native oxide are improved. Today, industrial anodization of aluminum products is a mature process which is widely applied as a measure to increase their performance.

Although great for corrosion resistance, the aluminum oxide film is a major obstacle when it comes to joining work pieces made of aluminum or aluminum alloys. To achieve good wetting of the two surfaces by the filler material, the oxide layer has to be removed. However, pure aluminum oxide has a high melting point (2072°C) and very good adherence to the underlying aluminum. One method for removing the oxide is flux brazing. This approach is problematic since furnace brazing with a flux contains vapor of dilute hydrochloric acid with minor amounts of hydrofluoric acid which creates a considerable amount of problems regarding work safety, environmental issues, and corrosion at the furnace. Another method is vacuum brazing which has been used for a small number of specialized applications such as in the aerospace industry. In the 1980s, aluminum products were increasingly considered for the automotive industry which lead to the development of furnace brazing with a flux under a protective atmosphere of nitrogen, known as the NOCLOK process [2]. Today, aluminum alloys excel through a strength-to-weight ratio which is comparable to steel, light-weight, and corrosion and weathering resistance.

Due to significant use of aluminum in industry and commercial products, there is a major research effort in this area. Therefore, several studies concerning the growth and structure of aluminum oxides at the atomic scale can be found, e.g. [3–8]. These studies have in common that they investigate the oxides formed under controlled conditions and/or using well ordered single crystal samples.

To understand changes in the microstructure during industrial relevant processes like heat-treatment, anodization, and corrosion, *ex-situ* studies on model systems are not sufficient. Investigating industrial processes under (or close to) realistic conditions can yield more relevant information although such studies increases the complexity of the experimental setup and data analysis. Using actual industrial materials instead of model systems introduces a number of challenges. For instance, using composite aluminum alloys instead of single crystals, more elements and structures in the sample have to be considered. The inhomogeneity of industrial samples with respect to microstructure, precipitates, constituent particles is also significant. Further, it is necessary to consider that each batch has a composition that is slightly deviating from the nominal composition.

To overcome all these challenges, a unique constellation from Swedish academia and aluminum industry has been assembled under the SSF-program *ALUminium oXides for processing and products* (ALUX) [9]. This project aims for an improvement of the corrosion resistance and versatility of aluminum products by combining the different skills from industry, theory and experimental science. My contribution to this project is within the experimental area as I am applying a range of synchrotron-based X-ray techniques for spectroscopy, microscopy and diffraction experiments to study aluminum and industrial aluminum products.

This licentiate thesis introduces a variety of aluminum based samples and synchrotron-based X-ray techniques to supply a background for the appended publications. The first publication reports how the variation of native oxide film thickness on pure and alloyed aluminum can be studied by X-ray reflectivity (XRR), X-ray photoelectron spectroscopy (XPS), and electrochemical impedance spectroscopy (EIS). All techniques shows a similar trend in thickness but the absolute values differ between the techniques. The second publication focuses on how the oxide layer changes during heating since these changes are crucial for the performance of brazing sheets. To achieve chemical and lateral resolution, a combination of spectroscopy and microscopy was used, mainly XPS and X-ray photoelectron emission microscopy (XPEEM). These publications demonstrate how synchrotron-based X-ray techniques shed light on industrial relevant systems.

## 2 Materials

Commercial aluminum products can be found everywhere in today's society and therefore there is an interest in improving the fundamental understanding of the interaction between aluminum and its alloying elements and the formation of the protective oxide layer on its surface. The oxide formation on aluminum has been studied for decades with a variety of surface science techniques, e.g. [3,5–8,10,11]. One major drawback with the conventional surface science approach is the use of model systems in controlled environments. Aluminum single crystals have been studied extensively but questions about the influence of alloying elements, heating and aqueous environments on the microstructure remain. Therefore, this thesis is aiming to extend the classical surface science approach by moving towards industrial alloys. Fig. 1 describes this transition graphically and illustrates how the complexity of the system increases and hence the demands on the experimental setup and data analysis.

This chapter will introduce the different types of aluminum samples that have been investigated in this thesis. The first section, 2.1, will describe the properties of pure single crystal and polycrystalline aluminum. Since aluminum has a high oxygen affinity it is almost always covered by an aluminum oxide layer. Therefore, aluminum oxides and their relevance with respect to industrial processes will be discussed in section 2.2. Moving towards more applied samples, section 2.3 will introduce the standards for wrought aluminum alloys with a special focus on the role of the different alloying elements and heat treatment of aluminum alloys. The last section (section 2.4) will explore the complicated interaction within composite aluminum alloys designed for brazing applications.

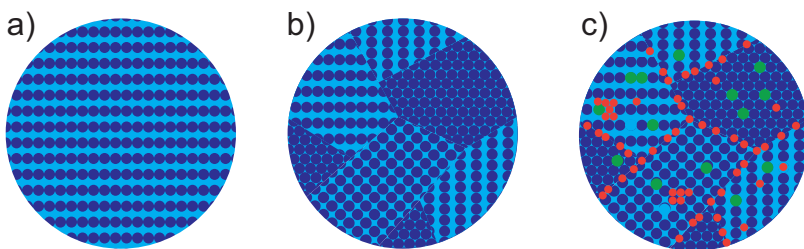


**Figure 1:** Models of a) an fcc (110) single crystal surface, b) a polycrystalline sample with different surface orientations c) a polycrystalline alloy with alloying elements at the surface. These models illustrate how the structures increase in complexity and hence create more challenges during data acquisition and analysis.

## 2.1 Pure Aluminum

Pure aluminum has a face centered cubic (fcc) crystal structure and a melting point of 660°C. The density of aluminum is low with  $\rho=2.7 \text{ g}\cdot\text{cm}^{-3}$ , which is about a third of the density of iron [12].

Another characteristic property of aluminum is its strong affinity to oxygen. Therefore, the most common ore of aluminum consists of a mixture of aluminum oxide, aluminum hydroxides, and oxyhydroxides. This type of ore is called bauxite and also contains varying amounts of iron oxides and silicates. Bauxite can be converted to aluminum oxide via the Bayer process [13]. In the Bayer process the aluminum oxide contained in the bauxite reacts with sodium hydroxide in a pressure vessel at a temperature of 150-200°C to form sodium aluminate. By cooling the filtered solution and passing carbon dioxide through it, aluminum hydroxide precipitates. Today it is more common to use a supersaturated solution of sodium aluminate seeded with aluminum hydroxide crystals to precipitate aluminum hydroxide, which is transformed into aluminum oxide by heating. The resulting alumina can then be smelted by electrolytic reduction, known as the Hall–Héroult process [14]. The Hall–Héroult process uses cryolite,  $\text{Na}_3\text{AlF}_6$ , to lower the melting point of alumina. Since the Hall–Héroult process requires large quantities of energy, recycling plays an important role in the aluminum industry today.

### Single Crystals

Aluminum single crystals are grown artificially by controlled phase transformation from the disordered liquid phase. Single crystals are common substrates for surface science studies since the geometrical arrangement of the atoms is clearly defined. This is the case because a crystal consists of atoms or a group of atoms arranged in a periodically repeating pattern in three dimensions.

The entire structure can hence be constructed by a translational displacement of the smallest repeating entity, the so called unit cell. The unit cell is defined by its lattice parameters, meaning the length  $a, b, c$  of the three independent cell edges and the angles  $\alpha, \beta, \gamma$  between these edges. Using the lattice vectors  $\vec{a}, \vec{b}, \vec{c}$  and translations operations the entire crystal structure can be defined by Eqn. 1.

$$R = n_1 \vec{a} + n_2 \vec{b} + n_3 \vec{c} \quad , \text{where } n_1, n_2, n_3 \in \mathbb{Z} \quad (1)$$

Originating from a lattice point, the positions of all atoms inside the unit cell are described by a set of vectors, see Eqn: 2.

$$r = x\vec{a} + y\vec{b} + z\vec{c} \quad , \text{where } 0 \leq m, n, o \leq 1 \quad (2)$$

The crystal structure of most metals is cubic meaning that the unit cell parameters  $a = b = c$  are equal and the angles are  $\alpha = \beta = \gamma = 90^\circ$ . By adding an atom in the center of the simple cubic unit cell, see Fig. 2 a), a body centered cubic unit cell is formed as shown in Fig. 2 b). Aluminum has a face centered cubic lattice and therefore atoms are not only placed on the corners of the unit cell but also at the center of each of the six faces, see Fig. 2 c).

The structure and orientation that a single crystal exhibits at the surface depends on how the crystal is cut with respect to the crystal planes. The intuitive way of describing the position of the planes would be by the ratio in which the axis are intercepted by the corresponding plane. The conventional way of denoting crystal planes is by the inverse of the interception between crystal plane and the

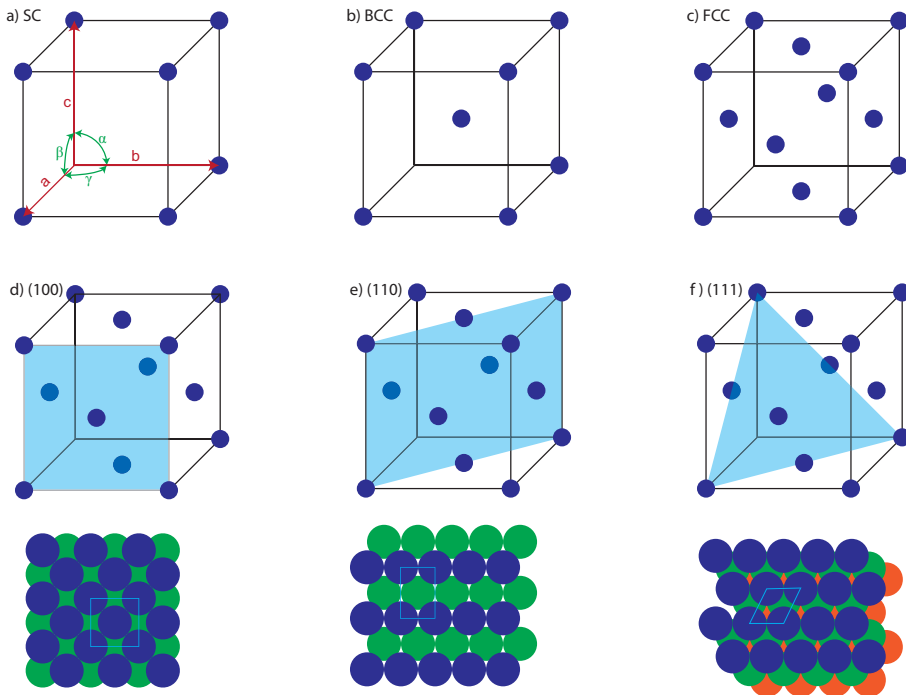


**Figure 2:** Illustrations of cubic units cells a) simple cubic, b) body centered cubic, c) face centered cubic and low index crystal planes d) (100), e) (110), f) (111) in a FCC crystal structure and the corresponding surfaces. In a cubic unit cell the cell parameters are equal ( $a=b=c$ ) and the angles are  $\alpha = \beta = \gamma = 90^\circ$ . The light blue lines in the bottom models describe the primitive surface unit.

axes defined by the lattice vectors. This index of the plane is represented by the three smallest integer combination in brackets (hkl). These indices are also referred to as Miller indices. Miller indices only containing values of one and zero are called low index planes.

## Polycrystalline Aluminum

The prefix *poly* come from ancient Greek  $\pi\omicron\lambda\upsilon\varsigma$  (polús) meaning many or much, hence polycrystalline aluminum consist of many entities of crystalline aluminum. The main difference between single crystal and polycrystalline aluminum is the presence of grain boundaries. Therefore, the mechanical and corrosion properties are different.

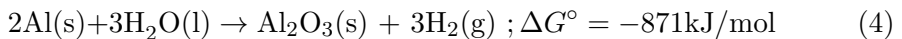
The grain size in polycrystalline aluminum varies greatly depending of the history of the sample (annealing, rolling, etc.) and can range from a few  $\mu\text{m}$  to several mm. The surface of a polycrystalline aluminum sample can exhibit random orientations for each single grain or the same orientation but laterally rotated towards each other. Samples of polycrystalline aluminum can be used as an intermediate step towards industrial materials since they contain grains and grain boundaries but no alloying elements.

## 2.2 Aluminum Oxide

As soon as aluminum is exposed to an oxygen containing environment it will form aluminum oxide. This can be explained by the large negative Gibb's free energy [15] for the reaction of aluminum with oxygen:



or the reaction of aluminum with water:



The thermodynamically stable and most dominant crystalline form of aluminum oxide is  $\alpha\text{-Al}_2\text{O}_3$  also referred to as corundum [16]. The structure of  $\alpha\text{-Al}_2\text{O}_3$  can be described as an hcp sublattice of oxygen anions with aluminum cations filling two thirds of the octahedral sites [17]. The lattice parameters of the unit cell are  $a = b = 4.7589 \text{ \AA}$  and  $c = 12.991 \text{ \AA}$ . An illustration of the  $\alpha\text{-Al}_2\text{O}_3$  unit cell is shown in Fig. 3.

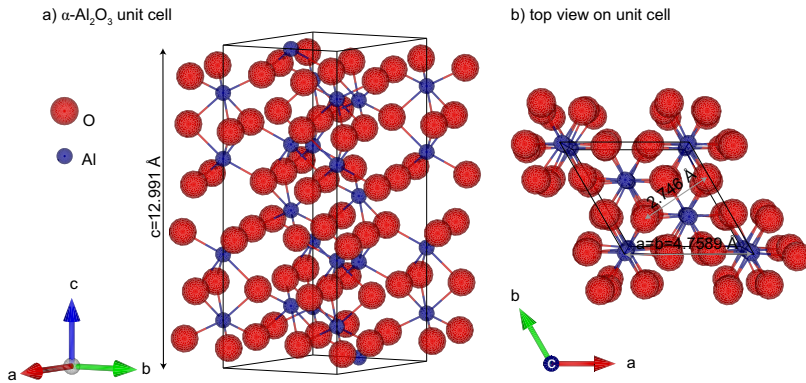


**Figure 3:** a) Unit cell of  $\alpha\text{-Al}_2\text{O}_3$  which consists of a hcp sublattice of oxygen anions and 2/3 of the octahedral sites filled with aluminum cations. b) gives a top view of the unit cell marking the lattice parameters  $a$  and  $b$  as well as the interatomic distance for the oxygen in the unit cell. Oxygen anions are represented in red and aluminum cations in blue. Illustration created by using VESTA [18] and the crystallographic data can be found in Ref. [17].

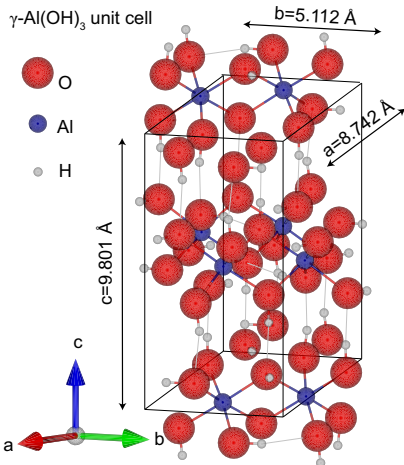


**Figure 4:** Model of a Gibbsite,  $\gamma\text{-Al(OH)}_3$ , unit cell. Illustration was created by using VESTA [18] and the crystallographic information can be found in Ref. [19].

Aluminum can form a range of meta-stable oxides. These can be divided into two subgroups, fcc and hcp, according to their arrangement of the oxygen anions. The different polymorphs of each of these two subgroups are obtained by varying the distribution of aluminum cations. Aluminum cations usually occupy octahedral or tetrahedral interstitial sites within the oxygen lattice. The close packing of four spheres creates a tetrahedral interstitial site and the closed packing of six spheres gives an octahedral site. The geometric arrangements leading to the formation of these two interstitial sites are shown in Fig. 5.

Alumina structures based on hcp packing of oxygen besides  $\alpha\text{-Al}_2\text{O}_3$  include  $\kappa$ -(orthorhombic) and  $\chi$ -(hexagonal) phases. Examples of fcc based alumina structures are  $\gamma$ -,  $\eta$  (cubic) and  $\theta$ -(monoclinic) phase.  $\gamma$ -alumina have received an increased research interest because of its catalytic activity.

Aluminum forms besides the oxides a wide range of hydroxides. Gibbsite and Bayerite are the most common structures of aluminum trihydroxides,  $\text{Al(OH)}_3$  whereas Boehmite and Diaspore are frequent monohydroxides,  $\text{AlOOH}$  [16].

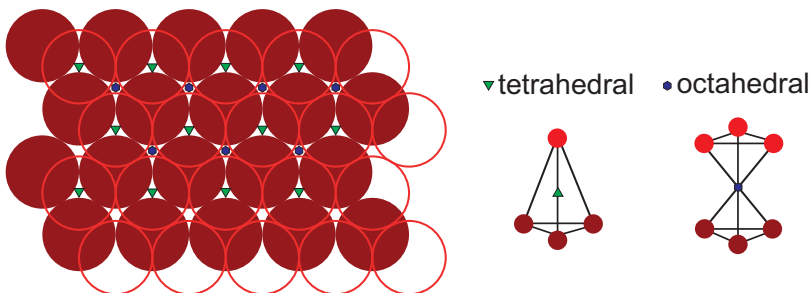


**Figure 5:** Model of hcp lattice with markers for tetrahedral and octahedral sites. Tetrahedral sites are marked with pink triangles and octahedral sites are marked with orange hexagons. Octahedra and tetrahedra are common building blocks for aluminum oxides and hydroxides.

Aluminum hydroxides typically consist of stacked oxygen double layers (O-Al-O) with aluminum occupying the octahedral interstitial sites. The hydrogen is usually arranged between the adjacent oxygen layers. As an example for the typical double layer structure of an aluminum hydroxide the unit cell for Gibbsite is shown in Fig. 4.

The above described aluminum oxides exhibit all a very well defined chemical and crystallographic structure. The native aluminum oxide film and anodic alumina films are usually amorphous and therefore they are not well described by conventional techniques for structural analysis. Nonetheless, these amorphous oxides play an important role concerning cohesion and stability of the interfacial bonding between the metallic aluminum and its protective oxide layer. Due to the strong cohesion between metal and oxide, aluminum has a naturally occurring abrasion and corrosion protection, which makes it a very utile metal.

Ultrathin films, films with a thicknesses of about 0.5 nm, of alumina have been studied on on several substrates including NiAl(110) [20, 21] and Ni(111) [22]. These combined with other studies [23] indicate that aluminum oxide can be grown on various substrates and that the building block found in ultrathin alumina films are similar to the ones at the surface of bulk alumina.

The native aluminum oxide film grown under ambient conditions, room temperature and atmospheric pressure, has a thickness ranging from 2-7 nm. It is usually described as an amorphous film that contains varying amounts of ordered oxide and hydroxide patches. By growing the aluminum oxide film at elevated temperatures the amorphous oxide growth begins to compete with the growth of  $\gamma$ -Al<sub>2</sub>O<sub>3</sub> since the Gibb's free energies of formation become nearly equal. Further, crystalline aluminum oxide is more likely to form on more densely packed surfaces of the substrate, hence more  $\gamma$ -Al<sub>2</sub>O<sub>3</sub> develops on Al(111) than on Al(100) or Al(110) [24].

The native aluminum oxide film provides aluminum products with a good corrosion resistance since the interface layer between aluminum and the oxide, the so-called barrier layer, has a very low conductivity for both electrons and ions which makes it an insulator for electrochemical reactions. The passive oxide film is essentially insoluble in pH-values ranging from 4.5 to 8.5. However, the exposure to corrosive environments, eg. seawater containing chlorides and sulfates, can lead to localized corrosion. To improve the corrosion protection in harsh environments the thickness of the alumina films can be increased. This can be realized by anodic anodization. During anodization aluminum is immersed into an acid electrolyte as part of an electrochemical cell. By applying an electric potential to the electrodes the following reactions can be driven to grow a thicker oxide layer. At the anode metallic aluminum is oxidized to aluminum oxide:



At the cathode hydrogen cations from the solution combine with electrons to form hydrogen gas:



Anodization of aluminum provides industry with a process to enhance the abrasion and corrosion resistance. Further, the approach provides a product finish with a high thermal stability. However, the excellent stability of alumina imposes a drawback in other applications of aluminum and its alloys.

One common application where the stability of alumina is an obstacle is brazing. During brazing the filler metal is heated above its melting temperature, for aluminum alloys around  $580^\circ\text{C}$ , between the work pieces. Then the filler is left to solidify into a joint between these work pieces. The major challenge for creating a good joint is to obtain a smooth continuous filling. This is only possible if the aluminum oxide covering the faying surface is broken up, so that the molten filler can easily wet the surfaces.

When considering an aluminum oxide film on aluminum, the alumina can only be broken by the difference in the thermal expansion coefficients since the liquidus of alumina is above  $2000^\circ\text{C}$ . The thermal linear expansion coefficient for aluminum is  $23.1 \cdot 10^{-6}\text{K}^{-1}$  and of alumina  $8.1 \cdot 10^{-6}\text{K}^{-1}$  at  $25^\circ\text{C}$  [25]. Hence, cracks in the aluminum oxide film will occur during heating.

To describe the break-up of the aluminum oxide layer on aluminum alloys several factors need to be considered. First of all, the alloying elements change the

thermal expansion behavior of the substrate. Secondly, alloying elements can act like dopants within the aluminum oxide film which affects the thermal stability of the film. Thirdly, alloying elements can diffuse towards the interface between alloy and oxide film, form particles, react with the oxygen in the film, and thereby expand and burst the oxide film. Each alloying element can therefore influence the way the alumina film is decomposing. Previous studies, e.g. [26,27], and the research presented in this thesis [28] show a major role of magnesium on the aluminum oxide break-up. The next section gives a general introduction to aluminum alloys and the influence of the alloying elements on the material properties of the alloy.

### 2.3 Aluminum Alloys

Combining aluminum with other elements creates an aluminum alloy. Typical alloying elements for aluminum alloys are copper, manganese, silicon, magnesium, iron, and zinc. Alloying requires that aluminum and the various alloying elements are mixed thoroughly while in a molten state. Common aluminum alloys contain up to 15 wt.% of total alloying elements. Wrought aluminum alloys are grouped into different series depending on their main alloying elements. The general series of the alloy determines the first of an assigned four-digit number, which identifies all industrial standard wrought aluminum alloys. Tab. 1 gives an overview over the different series. Each of the different standards has a defined composition range and hence characteristic properties.

To select the most suitable alloy for a distinct application in for example transportation, construction, or packaging one needs to consider other factors besides the chemical composition. These include amongst others if there is a possibility of strengthening the alloy in various ways, in which environment the alloys will

**Table 1:** The Aluminum Association alloy designation system for wrought alloys

Series	Major alloying elements	Heat treatable
1XXX	Al $\geq$ 99%	no
2XXX	Al-Cu-(Mg)	yes
3XXX	Al-Mn	no
4XXX	Al-Si	no/yes
5XXX	Al-Mg	no
6XXX	Al-Mg-Si	yes
7XXX	Al-Zn-(Mg)-(Cu)	yes
8XXX	Al-(other elements)	yes/no

be used, and if and how single workpieces should be joined.

The following sections will give an introduction to these considerations starting with the diverse roles of the alloying elements and continuing with how the alloys can be strengthened with a special focus on heat treatment. Finally the influence of the previous factors on the corrosion properties will be discussed.

## **Role of Alloying Elements**

By adding the correct amount of different alloying elements the properties such as strength, density, workability, electrical conductivity, and corrosion resistance can be greatly influenced. Not all elements in the alloy are deliberate additives but are rather impurities from the production or traces from the recycling process. Tab. 2 gives an overview of the composition of the different alloys used in the papers included in this licentiate thesis. It included three alloys of the 6XXX series, one alloy of the 7XXX series, and the base material and braze cladding of the brazing alloy.

Iron is the most common impurity in aluminum. The iron contamination originates from aluminum ore, which contains iron oxides, and from ferrous containers and tools used in the production. Iron has a high solubility in molten aluminum and therefore contamination easily occurs during the molten stages of production. On the other hand the solubility of iron in solid aluminum is very low, which makes iron form intermetallic particles often in combination with aluminum and silicon. In some alloys of the 1XXX series, iron is added intentionally to increase its strength slightly [29]. If iron and silicon are present in the alloy AlFeSi intermetallic particles form, whose exact compositions are under discussion.

Silicon is the main alloying element of the 4XXX series. It is commonly added to aluminum alloys to lower their melting point and to improve the fluidity of the melt and therefore finds applications as braze claddings or welding wires. Silicon has a low solubility in aluminum at room temperature and at 12.5 wt.% silicon it forms a eutectic with aluminum [29]. In the 6XXX, series silicon and magnesium are the main alloying elements. Levels up to 1.5 wt.% are used to produce  $Mg_2Si$  (magnesium silicide) precipitates during age hardening, the fine precipitates increase the strength [1]. The intermetallic  $Mg_2Si$ -particles can however also influence the local corrosion or anodization of aluminum alloys [30].

Magnesium is also used on its own as a major alloying element in the 5XXX series. Maximum 17.4% of magnesium can be dissolved in aluminum [29] but

**Table 2:** Chemical composition of aluminum alloys which were investigated in this thesis. FA7856 and FA7825 are custom made alloys used in brazing sheets. Quantities given in wt.%. Aluminum is remainder for all alloys.

	Si	Fe	Cu	Mn	Mg	Cr	Zn	Ti	Bi
AA6005	0.50-0.90	0.35	0.30	0.50	0.40-0.70	0.30	0.20	0.10	–
AA6060	0.03-0.60	0.01-0.30	0.10	0.10	0.35-0.60	0.05	0.15	0.10	–
AA6063	0.02-0.60	0.35	0.10	0.10	0.45-0.90	0.10	0.10	0.10	–
AA7075	0.40	0.50	1.2-2.0	0.30	2.1-2.9	0.18-0.28	5.1-6.1	0.20	–
FA7856	9.7	0.22	–	–	0.67	–	–	–	0.08
FA7825	0.16	0.22	0.33	0.83	0.23	–	–	0.16	–

usually not more than 5.5% of magnesium are used in wrought aluminum alloys. Due to the high solubility of magnesium, the alloys can be strengthened by solid solution hardening. By this treatment, aluminum-magnesium alloys obtain their high strength and corrosion resistance. Aluminum alloys containing more than 3% of magnesium have a tendency to precipitate the intermetallic compound  $\beta$ -Al<sub>8</sub>Mg<sub>5</sub> at grain boundaries [12].

Other important alloying elements include copper, which increases strength and hardness, chromium, which is used in aluminum-magnesium alloys to prevent grain growth and recrystallization in aluminum-magnesium-silicon during heat treatment. However, an excess of chromium (Cr>0.35%) leads to the formation of coarse constituents with other alloying elements. Manganese is used to produce moderate strength non-heat treatable alloys of the 3XXX series. The combination of zinc with other alloying elements such as copper and magnesium leads to high strength heat treatable alloys.

The role of alloying elements within the bulk of aluminum alloys has been studied extensively because of its industrial importance. The local effect of the various alloying elements on the surface layer has however not been investigated equally thoroughly. This is surprising, since the understanding of the surface behavior is important for applied processes such as abrasion, anodization, brazeability, corrosion, and optical appearance amongst others. To gain more relevant information on the behavior of the oxide film, recent studies focused on conducting experiments *in-situ* during anodizing, heating or in contact with liquids [28, 30–32].

## Strengthening

Mechanical and thermal treatments have a great impact on the mechanical and technological properties of aluminum and its alloys. To distinguish which strengthening method was applied to the alloy, temper designations are used. F marks alloys that are kept as fabricated whereas O stands for annealed wrought alloys.

H means strain hardening, which is a common way of strengthening non-heat treatable aluminum alloys. Strain hardening, which is also referred to as work hardening, moves dislocations, changes within the crystal structure, by plastic deformation to increase the strength. The grain size is changed by strain hardening, too.

Solid solution strengthening is based on internal strains that are generated when atoms of one metal are introduced into the crystal lattice of another metal. The solute atoms can either occupy interstitial sites or they can substitute for solvent atoms in the lattice site. The factors governing the substitutional solubility in alloys are commonly referred to as the Hume-Rothery rules. They state that the size difference between the two atoms should be 15% or less, the crystal structure should be similar, and valency and electronegativity should be similar to be soluble in a larger extent [12]. The strengthening effect on the other hand is greater if the difference between the atomic radii is dissimilar because it poses a larger strain in the lattice.

The solubility of other phases in aluminum is crucial to precipitation strengthening which can be part of a heat treatment and therefore has the temper designation T. Wrought alloys from the 2XXX, 6XXX, and 7XXX series are often age hardened. That means that a second phase is dissolved in the aluminum by heating the alloy typically above 450°C and then rapidly quenching it to create a supersaturated alloy. By holding the supersaturated solid solution at a temperature below the solvus<sup>1</sup> the second phase will try to reach equilibrium and thus start precipitating. This process is also referred to as aging. If the alloy is kept at a too high temperature, coarse precipitates can form that do not result in the desired strengthening effect. Fig. 6 shows a schematic representation of precipitation strengthening. Common precipitates for alloys of the 6XXX series are Mg<sub>2</sub>Si and FeSiAl particles. The 7XXX series forms amongst others MgZn<sub>2</sub> and Mg<sub>2</sub>Si [12].

Other particles influencing the strength and other properties are dispersoids and constituent particles. Dispersoids are particles comprised of elements that have

---

<sup>1</sup>A line on a phase diagram which defines the limit of solid solubility.

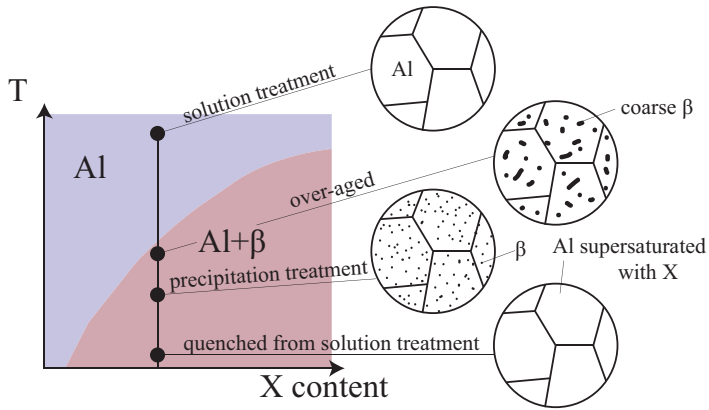


**Figure 6:** Generic phase diagram representing the different stages of a solution treatment followed by a rapid quenching and aging. By heating an aluminum alloy above the solvus temperature, a second phase, here shown as  $\beta$ , can dissolve in it. This second phase can be retained in the solution by rapid quenching and aged at a specific temperature to form precipitates of the desired size. If the second phase forms coarse precipitates the alloy is called over-aged.

a very low solubility in aluminum. Their typical size ranges from  $0.05 - 0.5\mu\text{m}$ . Constituent particles are much larger, reaching sizes of  $10\mu\text{m}$ . They are formed most often by alloying elements such as Fe, Si, Mn, and Mg.

The occurrence of any of the described particles can greatly influence the strength of aluminum alloys but they also affect the oxide layer growth when formed in the surface near region.

## 2.4 Brazing Sheets

Work pieces can be joined by different processes, e.g. mechanical joining and adhesives. Hot joining processes include soldering, brazing, and welding. Brazing is defined as a hot joining process in which temperatures above  $450^\circ\text{C}$  but below the solidus<sup>2</sup> of the parent material are used. It is used in applications that require a permanent joint with similar strength and thermal conductivity to the parent material. Work pieces with either very thin or very thick cross section or assemblies with a large number of joints are also often brazed.

A typical brazing sheet is a composite material which consists of a core alloy and a braze cladding. The core has a higher melting temperature and therefore can maintain the structure while the braze cladding can be melted selectively. The liquid phase is then drawn between the different close-matched work pieces

<sup>2</sup>The solidus is the highest temperature at which a phase is completely solid.

by capillary forces. Upon cooling, a solid joint between the workpieces is formed by the braze cladding.

For aluminum alloys the braze cladding typically consists of an aluminum-silicon alloy since the silicon lowers the melting temperature. The surface of the brazing sheet is covered of a native aluminum oxide film, see Fig.7. The aluminum oxide has a greater thermal stability than the braze cladding and the core alloy and therefore it is important to know at which temperature the aluminum oxide layer breaks up, and how the surface changes during melting of the braze cladding. This is the case because the surface has a major influence on the wetting, the ability of the liquid phase to stay in contact with the solid phase, and the capillary effects, which pull the liquid into the space between the work pieces.

Brazing of aluminum can be done either with a flux or in vacuum. Fluxes can be applied to the brazing alloy in form of a powder, a paste, a liquid, or vapor. They are applied to the brazing sheet to remove the surface oxide layer. Vacuum brazing is considered to be a fluxless brazing method which is performed in vacuum furnaces that maintain pressures around  $10^{-5}$  mbar. The advantages of vacuum brazing are the absence of corrosive fluxes in the furnace, the possibility to form a large number of joints, the option to perform hardening in the same furnace, and the high repeatability of the brazing result.

The brazing sheet that was investigated in this thesis was designed for vacuum brazing. This particular composite alloy finds application in heat exchangers. How the single brazing sheets can be assembled to form parts of a heat exchanger is shown in Fig. 7. The composition of the brazing sheet is given in Tab. 2. There it is shown that the braze cladding FA7856 has a significantly higher content of Si and Mg than the core material FA7825. Si was added to the braze cladding to lower the liquidus and Mg is needed for facilitating the decomposition of the aluminum oxide film.

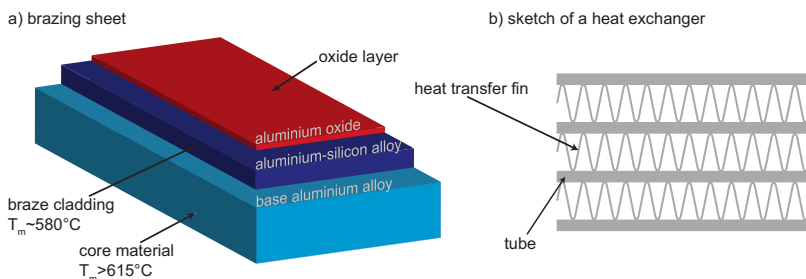


**Figure 7:** a) illustration of a typical composition of a brazing sheet and b) sketch of assembly of brazing sheets for a heat exchanger which can be found e.g. in heat exchangers in cars.

## 3 Instrumentation and Methods

This chapter gives a description of the different surface science techniques used in the present thesis. Since the experimental methods are based on the use of X-rays, the chapter begins with a short introduction into X-rays and their generation in a synchrotron (section 3.1). This is followed by the description of the different experimental methods based on reflection (section 3.2), spectroscopy (section 3.3), and microscopy (section 3.4).

### 3.1 X-rays and Synchrotron Radiation

W. C. Röntgen studied the phenomena occurring when an electric current passed through a gas of extremely low pressure in 1895. This work led to the discovery of an unknown type of radiation, X-rays, which are also named after him in some languages, e.g. German and Swedish. Röntgen's work was followed by W. H. Bragg and W. L. Bragg's discovery that crystalline samples produced a characteristic diffraction pattern when irradiated by X-rays, and later M. von Laue's description of X-rays as waves in 1912. All four scientists received a Nobel prize in physics for their work. These discoveries have enabled scientists to probe and interpret the crystalline structure of materials at the atomic level. Since their discovery, X-rays have become an important source for a wide range of experiments in all fields of natural science.

Conventional X-rays are produced by bombarding a metal target with high-energy electrons from a glowing filament. The X-rays generated in this way consist of a broad spectrum due to bremsstrahlung with additional sharp lines from electronic transitions. These transitions occur when the bombarding electron has sufficient energy to eject an inner shell electron from the metal target creating an electron vacancy. To fill the low level vacancy, an electron from a higher level deexcites and a photon is emitted with a sharply defined energy related to the energy difference between level of the vacancy and the initial energy level of the electron. These emission lines are characteristic for every element. Common metal targets for X-ray lab sources are Mo and Cu. To obtain a well defined X-ray energy, monochromators are used.

Classical electrodynamics describes how charged particles that are accelerated emit energy in form of electromagnetic waves. The total power radiated of non-relativistic particles is very small and scales only with the square of the change of the charged particles momentum, as described by Larmor [33].

In synchrotrons, relativistic particles are used. Thus, they need to be described

by relativistic electrodynamics. This is done by applying a Lorentz transformation to time and momentum. By further considering, that the charged particles are accelerated on a circular path, as in a bending magnet, the following expression can be derived, as done by Liénard [34], where  $c$  is the speed of light in vacuum,  $\varepsilon_0$  the permittivity of free space and  $R$  the bending radius of the orbit the accelerated particle

$$P_s = \frac{e^2 c}{6\pi\varepsilon_0} \frac{1}{(m_0 c^2)^4} \frac{E^4}{R^2} \quad (7)$$

In equation 7 the radiated power,  $P_s$ , for particles with the elementary charge,  $e$  is proportional to the fourth power of the particle energy,  $E$ , and inversely proportional to the fourth power of the rest mass,  $m_0$ . Thus, mostly particles with a low rest mass, usually electrons, at relativistic velocities are used to produce synchrotron radiation.

By combining several short bending magnets with alternating polarity into an undulator or wiggler, the electrons are forced onto an sinusoidal path, which allows for the production of a more intense and highly collimated radiation. Today, dedicated storage rings are used instead of synchrotrons because they operate at constant energy and thus, provide a more stable beam.

All in all the advantages of using synchrotron radiation sources are high intensity, good tunability with respect to the wavelength, low divergence and a small beam size. A more complete description can be found here [35, 36].

## 3.2 X-ray Reflectivity

X-ray reflectivity (XRR) is used to study the structure of surfaces, interfaces, and thin films. With XRR, information on the roughness and the thickness of a sample can be derived in a non-destructive manner down to a few hundreds of a nm. It can also be applied to measure the density of different layers. In contrast to X-ray diffraction, XRR is not limited to crystalline samples.

In XRR, the sample is irradiated with a monochromatic X-ray beam with a wavelength  $\lambda$  at an incident angle of  $\alpha_i < 5^\circ$ . These X-rays are then partially reflected at the surface or an interface at an angle of  $\alpha_f = \alpha_i$ . The reflected intensity is recorded as a function of the incident angle  $\alpha_i$ . Typically, the angle is reported as the angle between incidence angle and the surface in contrast to conventional optics.

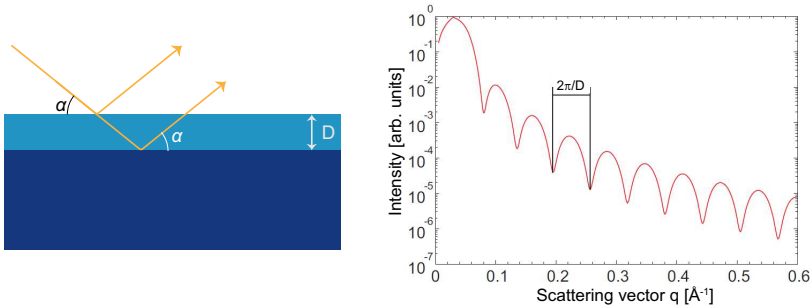


**Figure 8:** Illustration of XRR from a thin layer on a substrate and a typical reflectivity curve.

To describe the reflectivity of a material the complex refractive index  $n$  is used. It is defined as

$$n = 1 - \delta + i\beta \quad (8)$$

where  $\delta$  and  $\beta$  represent material specific constants proportional to the electron density and absorption. Typical values for  $\delta$  are in the range of  $10^{-6}$ , which is about two orders of magnitude larger than usual values for  $\beta$ .

Generally total reflection can be observed at angles below the critical angle,  $\alpha_c$ . At angles above  $\alpha_c$  the specularly reflected intensity decays.

The first reflection of X-rays originates at the interface between vacuum and the sample's surface. If the incidence angle is sufficiently small the total intensity will be reflected because the refractive index of the medium is smaller than the one of vacuum. Since air has a low density this approximately hold true for experiments in air, too. The critical angle  $\alpha_c$  is usually below  $1^\circ$  for vacuum(air)/medium interfaces.

At angles higher than the critical angle the reflected intensity decreases rapidly with a  $\frac{1}{q^4}$  dependency, where  $q$  is the scattering vector. Oscillations in intensity, Kiessig fringes, superimposed onto the decaying curve can be observed, as shown in Fig. 3.2. These originate from the interference of X-rays that have been reflected from another interface in the sample. The periodicity of these oscillations can be used to determine the thickness of the different layers in the sample.

$$D = \frac{2\pi}{\Delta q} \quad (9)$$

A more detailed descriptions of XRR can be found in the literature, e.g. [37].

### 3.3 Spectroscopy

The term spectrum was coined in an scientific context by Sir Isaac Newton when describing how visible light is dispersed through a prism. Later the meaning of the term was expanded to cover the whole range of electromagnetic radiation. Today the term spectroscopy refers to measurements of a response to a certain varying stimulus, e.g. photons and electrons.

This section introduces two spectroscopic techniques based on X-rays, namely X-ray Photoelectron Spectroscopy (XPS) and X-ray Absorption Spectroscopy (XAS). The phenomena introduced here are also used to create images in X-ray Photoelectron Emission Microscopy (XPEEM) as described in the microscopy section 3.4.

#### X-ray Photoelectron Spectroscopy

XPS is one of the most commonly used techniques to study the chemical composition of surfaces. It is based on the concept behind of the photoelectric effect, which was discovered by H. Hertz in 1887 [38]. The photoelectric effect is the name for the process of removing an electron from the surface of a solid by irradiating it with photons. A. Einstein [39] explained this phenomenon in 1905 and later, in 1921, he was awarded the Nobel Prize in physics "for his services to Theoretical Physics, and especially for his discovery of the law of the photoelectric effect" [40].

K. Siegbahn discovered that the core level binding energy of an electron in an atom is influenced by the chemical surroundings of the photoemitting atom and he coined the term Electron Spectroscopy for Chemical Analysis (ESCA) [41]. In 1981 K. Siegbahn received the Nobel Prize in physics "for his contribution to the development of high-resolution electron spectroscopy" [42]. Since the chemical surrounding of the atom can be deduced from an XP spectrum, XPS measurements give information on the electronic and chemical state of the atom.

Typical XPS measurements use X-rays in the energy range from 10 to 1000 eV. Even though X-rays at these energies can penetrate the sample up to several  $\mu\text{m}$ , the photoelectrons emitted originate only from the topmost layers of the sample. This is due to the short inelastic mean free path of electrons in solid materials as shown in Fig. 9 a). This means that e.g. photoelectrons emitted with a kinetic energy of 100 eV from solid aluminum originate from the topmost 5 Å of the sample [43].

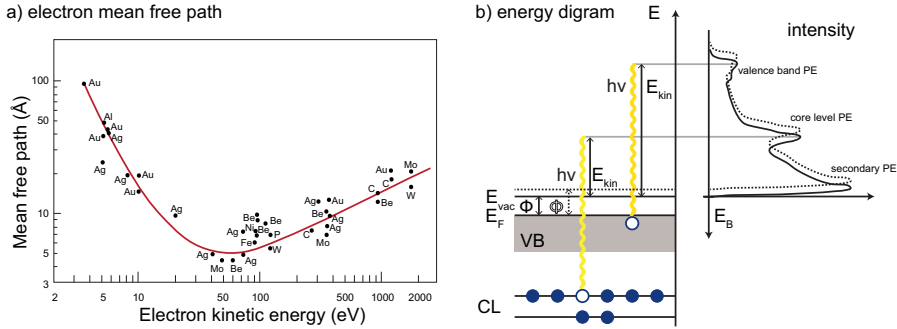


**Figure 9:** a) Universal curve for the electron mean free path as function of the kinetic energy. It explains why electron based methods are very surface sensitive in the energy range of 10-2000 eV. b) Energy diagram illustrating the principle of the core-level photoemission process. A photon with an energy of  $h\nu$  impinges the surface and is absorbed by a core-level electron. After the excitation the electron is transported to the surface and overcomes the vacuum barrier  $E_{vac}$  and to becomes a free electron, which has a kinetic energy of  $E_{kin}$ .

The processes taking place during an XPS experiment are shown in Fig. 9 b) and can be explained in a classic way by the simplified three step model [44]. In the first step a photon with an energy of  $h\nu$  impinges the surface and excites an electron with the initial energy  $E_i$ . After the excitation the electron is transported to the surface and has a final state energy of  $E_f$ . Finally, the electron has to overcome the vacuum barrier and becomes a free electron, which has a kinetic energy of  $E_{kin}$ . Invoking the law of conservation of energy, the following equation can be deduced

$$E_i + h\nu = E_f + E_{kin} \quad (10)$$

$$E_{kin} = h\nu - E_B - \Phi \quad (11)$$

By considering that the difference between the initial energy  $E_i$  and the final energy  $E_f$  is equal to the ionization potential  $E_I$ , which itself is equal to the sum of binding energy  $E_B$  and work function  $\Phi$  of the sample, we can rearrange equation 10 to arrive at 11. From that it is clear that by detecting the kinetic energy,  $E_{kin}$ , it is possible to extract the binding energy,  $E_B$ , if a monochromatic light source with a known photon energy,  $h\nu$ , is used and the sample is kept at the same potential as the analyzer, the sample Fermi level,  $E_F$ .

XP spectra are created by plotting the detected intensity of photoelectrons as a function of the kinetic energy  $E_{kin}$  or binding energy  $E_B$ . Variations in binding energy, known as chemical shifts, can be used to deduce the chemical state of the

photoemitting core-level atom. Chemical shifts are often related to the charge that the emitting atom is carrying. Therefore, chemical shifts to higher binding energies are often caused by an increased positive charge. The relation between core-level, kinetic energy and shift in the XP spectrum is illustrated in Fig. 9 b). A more rigorous treatment of the theoretical background on photoionization can be found e.g. in Ref. [44–46].

## X-ray Absorption Spectroscopy

The excitation of a core-level electron can lead to the emission of a photoelectron into the vacuum as in XPS or it can result in a bound electron being transferred into an unoccupied state in the conduction band, which is the case in XAS, see Fig. 10. Typically a XAS measurement is carried out by scanning across the absorption edge of the element of interest.

Since it is often experimentally easier to detect photoelectrons rather than photons, XAS measurements use an indirect way of obtaining the signal via the core hole decay. The core hole can either be filled through fluorescence decay or Auger decay. During fluorescence decay the core hole is filled by a valence electron transitioning into the lower energy state and releasing the excess energy by radiation. In Auger decay a valence electron fills the core hole but the excess energy is transferred to another electron which then has a sufficient energy to leave into the vacuum, see Fig. 10. Since the number of core holes created by the initial X-ray absorption is proportional to the emitted electrons from the Auger decay, their signal can be used to measure the absorption signal [47].

XA spectra in Auger decay mode are generated by detecting the intensity of the Auger electrons as a function of photon energy. Since these spectra are char-

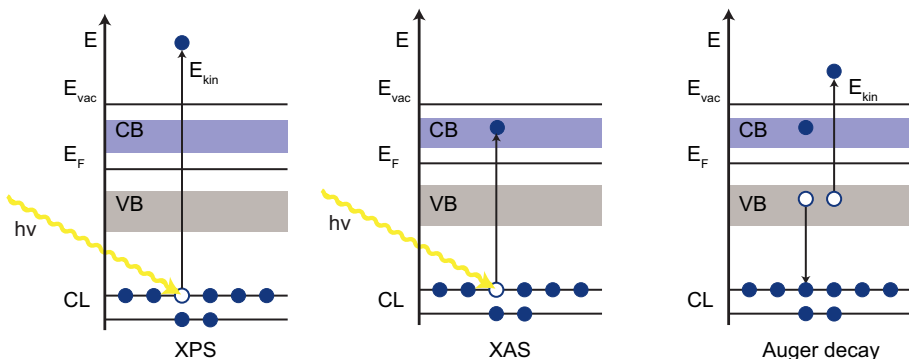


**Figure 10:** Energy diagrams comparing XPS, XAS, and Auger decay.

acterized by transitions to unoccupied states, they contain information about the chemical state as e.g. the oxidation state. Collecting parts of the absorption spectrum at energies lower or higher energies than the absorption edge gives Near-Edge X-ray Absorption Fine Structure (NEXAFS) and Extended X-ray Absorption Fine Structure (EXAFS). These can provide information on coordination number and interatomic distances [48].

### 3.4 Microscopy

The term microscopy comes from the two Ancient Greek words *μικρός* and *σκοπεῖν*, which mean "small" and "to see", hence microscopy aims to observe objects that cannot be resolved by the naked human eye. The tools that the field of microscopy provides for doing so range from simple magnifying glasses to the traditional optical light microscopes to microscopes that can resolve structures on a nanometer scale. Two major groups of those include electron microscopes like scanning electron microscopes (SEM) and scanning probe microscopes such as scanning tunneling microscopes (STM) and atomic force microscopes (AFM).

The set of microscopy techniques that were used in this thesis belong to the group of cathode lens microscopy. The different microscopy types are referred to as cathode lens microscopy since the sample is negatively biased. However, a wide range of electrons can be used for imaging, e.g. reflected electrons, elastically or inelastically scattered electron, thermionic emitted electrons, and (X-ray) photoelectrons [49]. The presented work includes data from measurements performed at the SPELEEM (Spectroscopic PhotoEmission and Low Energy Electron Microscope) from Elmitec GmbH [50], that was situated at the soft X-ray beamline I311 and has been transferred to the new synchrotron facility MAX IV Laboratory in Lund. The synchrotron is used as a tunable X-ray source providing radiation in the energy range of 45 eV to 600 eV. A schematic describing the general layout of the SPELEEM is shown in Fig. 11. A in depth coverage of the historic development and theoretical concepts behind cathode lens microscopy can be found in Ref. [51], a book written by one of the inventors of LEEM and PEEM, Ernst Bauer. The following section will give an introduction to the cathode lens microscopy techniques, namely mirror electron microscopy (MEM), low energy electron microscopy (LEEM), and X-ray photoemission electron microscopy (XPEEM).

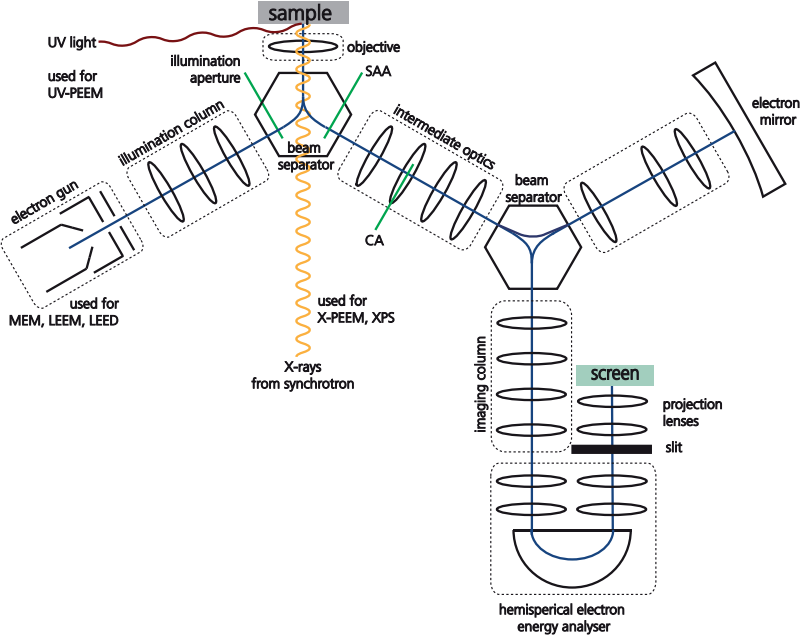


**Figure 11:** Schematic of the AC-SPELEEM setup now situated at the MAXIV laboratory. There are three different sources for imaging: an UV-light source for UV-PEEM, an electron gun for MEM, LEEM, and LEED, and X-rays from the synchrotron for XPEEM, and XPS. The electron trajectories are marked in blue, the ellipses depict electron lenses. The slit after the energy analyser can be used to select photoelectrons with a selected energy. (The aberration correction column with the electron mirror was added after the data presented in paper II was collected.)

## Mirror Electron Microscopy

When operating the SPELEEM in MEM mode, the electrons emitted from the Lanthanum Hexaboride ( $\text{LaB}_6$ ) cathode are accelerated to 20 keV in the electron gun. On the way to the sample the electron beam is focused in the illumination column by the condenser lenses. The illumination aperture can be used to adjust the area of the sample that should be illuminated by the electron beam. The magnetic beam separator (sector field) deflects the electron beam by  $60^\circ$  towards the sample, see Fig. 11. The electrons are accelerated towards the sample with very low kinetic energies. The sample itself has a potential of -20 kV-SV (start voltage). The negative SV in MEM causes the sample to act as an electrostatic mirror, hence the name mirror electron microscopy. This means that the electrons are reflected by an equipotential surface several nanometers above the real surface [52]. By adjusting the strength of the condenser lenses the Gaussian image plane, shown as IP in Fig. 13 b), can be projected onto the detector screen, which in this instrument is a MCP (micro-channel plate)

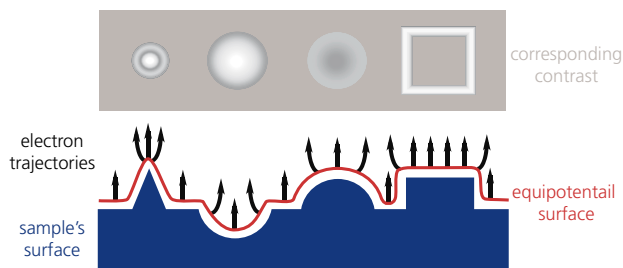


**Figure 12:** Examples of how the topography of the surface affects the contrast in the resulting MEM image. Features on the surface create local fields that cause deviation in the photoelectrons path leading to an altered contrast in the resulting image. (according to [55,56])

detector with a CCD (charge-coupled device) camera.

The contrast in the MEM image is caused by local fields at the surface originating from features and work function differences, see Fig. 3.4. These disturb the trajectory of the electrons on the way towards and back from the equipotential surface [53]. The exact contrast formation and resolution in MEM is still under discussion, a recent comparison between different imaging theories can be found here [54]. Both experimental and theoretical work suggest that the depth resolution in MEM is significantly better than the lateral resolution, which makes MEM sensitive to topographic height variations [51]. MEM is a very useful imaging mode for amorphous surfaces since it is not based on diffracted electrons in contrast to LEEM.

## Low Energy Electron Microscopy

In LEEM mode the electrons actually interact with the sample's surface due to the positive SV as in contrast to MEM mode, see Fig. 13 a). However, the electrons are still retarded to low energies, typically from ranging from 5 to 100 eV. These electrons will then be diffracted by the sample's surface. After the interaction with the surface at low energies the electrons are reaccelerated to 20 keV to enable the focusing by the electromagnetic lenses on their path to the detector. By either projecting the back focal (diffraction) plane (BFP) or the Gaussian image plane (IP) onto the screen the Low Energy Electron Diffraction (LEED) pattern or the real space LEEM image can be detected.

By inserting a contrast aperture (CA) into the BFP a specific diffraction spot can be selected for imaging, see Fig. 13 b). If the CA is positioned around the (0,0) diffraction spot, the image is collected in bright field LEEM. Bright field LEEM images obtain their contrast from the differences in composition

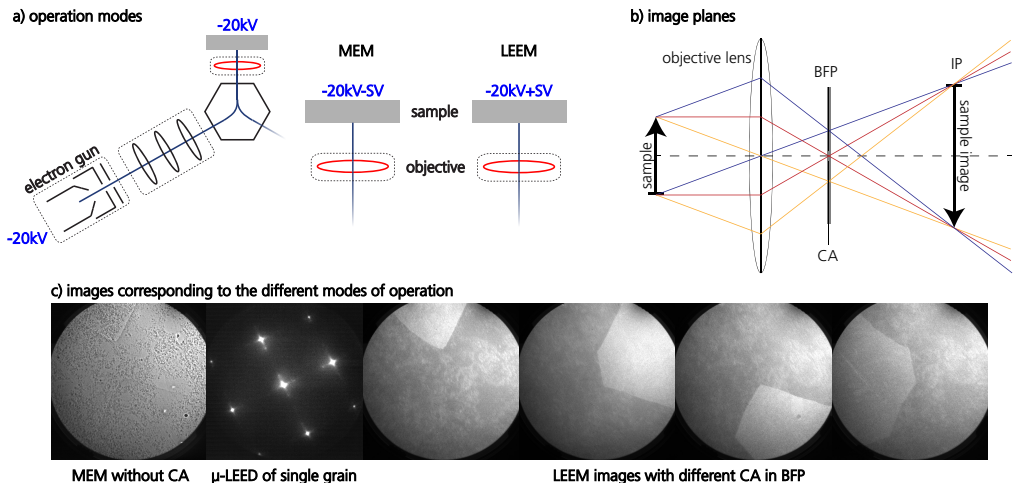


**Figure 13:** a) Schematic drawings comparison between operating modes MEM and LEEM. In MEM a negative SV is applied to the sample leading to reflect the electron beam several nanometers above the surface. If a positive SV is applied the low energy electrons are diffracted at the surface and either the (0,0) or another diffraction spot can be selected for imaging leading to bright field and dark field LEEM images. b) Sketch of image planes. In the BFP the diffraction pattern is formed and in the Gaussian IP the real space image is created. c) Comparison between different imaging modes.

and structure of the sample. By selecting another diffraction spot, areas of the sample with the same structure as the chosen diffraction spot, will appear bright in the LEEM image. This technique is referred to as dark field LEEM. It is very useful to identify the abundance of a specific structure or to distinguish different domains. The spatial resolution in non-aberration-corrected LEEM is typically better than 10 nm. New aberration-corrected LEEMs can reach a spatial resolution of 2 nm [57].

Fig. 13 c) compares images of the same sample taken in different modes. The leftmost displays a very flat sample topography in MEM mode, the second to the left shows a  $\mu$ -LEED pattern of one of the grains, the four following images depict LEEM images acquired with different contrast apertures.

## Photoelectron Emission Microscopy

In Photoelectron Emission Microscopy (PEEM) the sample is illuminated with a relatively wide photon beam, photoelectrons are emitted from the whole illuminated area and refocused into a real space image. The sample can be illuminated with different photon energies which then give rise to various excitation and emission processes.

In the SPELEEM setup the sample can be illuminated with photons from a UV-lamp or with undulator radiation from the synchrotron. The UV-lamp emits photons with an energy of 5 eV. The undulator can be tuned to provide photons within an energy range of 45-1500 eV [58], whereof photons with energies up to 600 eV are transmitted to the microscopy branch. To select a narrow wavelength range of the synchrotron radiation a modified SX-700 monochromator is used before the light enters the SPELEEM.

If photons with low energies are used to excite the sample only electrons from the highest occupied energy level/ valence band are emitted. The resulting photoelectrons have a low kinetic energy. Photoelectron with low kinetic energies can also be generated by secondary events. This means that the primary photoelectron underwent inelastic scattering and thereby transferred energy to a secondary electron. Since inelastic scattering can occur multiple times several secondary electrons can be created by one original excitation and the secondary electrons themselves can undergo inelastic scattering leading to a cascade. Secondary electrons have lost the information about the primary excitation event. However, they can be used for imaging the work function contrast. A difference in work function arises from a difference in chemical composition/ doping. This difference is then seen in the onset of the secondary electron, see Fig. 9 b) solid vs. dotted line, which causes the main contrast in the resulting PEEM image together with contributions from the topography.

To obtain a chemical contrast in the PEEM image, photons with a higher energy, X-rays, are used to emit core-level electrons. A description of the photoexcitation process was given previously in section 3.3. To image a certain element a photoexcitation energy above the core-level binding energy of the desired elements is chosen and the SV is adjusted to fulfill Eqn. 12. Using the hemispherical energy analyzer a small energy range of photoelectrons are chosen for imaging.

$$E_B = h\nu - SV - \phi \quad (12)$$

This results in XPEEM images displaying areas with a high concentration of the chosen species as bright spots [59]. This allows to directly identify spatial distribution of a specific atom or ion. The probing depth in XPEEM is up to 5 nm as determined by the electron inelastic mean free path. The lateral resolution of XPEEM images is slightly less than the one achieved in LEEM and is typically around 10 nm. Since the amount of emitted photoelectrons is much lower than the one of secondary electron XPEEM images are obtained with a longer acquisition time to get a similar count.

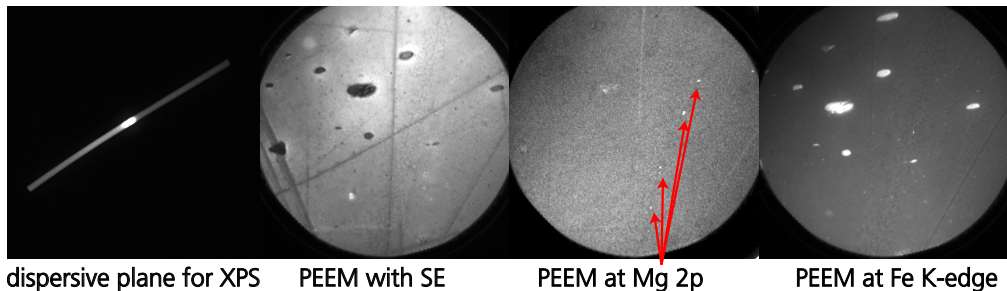


**Figure 14:** Imaging modes using the energy analyzer. Left image of the dispersive plane used to create XP spectra, here an Al 2p core-level spectrum of AA6063. Followed by PEEM images of the same alloy with different imaging modes. Left PEEM with secondary electrons using mostly a work function and topography contrast, center showing a chemical contrast corresponding to the Mg 2p core-level, left XPEEM image obtained in absorption mode at the Fe K-edge.

Fig. 14 shows three different PEEM images obtained from the same sample area. The leftmost PEEM image has a contrast mainly from work function and topographic differences, whereas the center and right image have mainly an element specific contrast. The center image was recorded using the Mg 2p core-level binding energy and shows small Mg particles segregated along the grain boundary. The rightmost image was acquired by using the Fe K-absorption edge, which enables the identification of large Fe-rich particles on the surface.

XPEEM in absorption mode follows the physical principles described previously for XAS, see section 3.3. Since in XAS mode secondary electrons with typically energies of less than 10 eV are emitted and the IMFP increases with lower energies, see Fig. 9 a), the probing depth increases to up to 10 nm.

Within the different modes of imaging with PEEM there are several factors contributing to the image contrast: work function, chemical composition, surface orientation, electronic structure, local electrostatic fields, areas of altered conductivity, partial charging and magnetic domains. Each of these material properties affects the contrast but to a varying extent depending on which mode of operation is chosen, e.g. the contribution of work function contrast is high when using low excitation energies but very weak at high excitation energies [55]. Additionally, the topography of the surface influences the contrast. Features, e.g. scratches and particles on the surface, alter the potential and lead to deflection, focusing or defocussing of the photoelectrons. How these local fields affect the images is also depending on other experimental parameters, e.g. accelerating voltages [56].

A review on the historic development of XPEEM over the past decades can be found here [60] and an overview on recent advances in the field is given in [61].

## 4 Summary of Papers

The work presented in this thesis demonstrates the successful application of classical surface science techniques to model samples as well as to industrial materials. Paper I combines XPS and XRR with Electrochemical Impedance Spectroscopy (EIS) to determine the oxide thickness on several aluminum single crystals and industrial aluminum alloys. Paper II uses XPS and a range of cathode lens microscopy techniques to follow the decomposition of the aluminum oxide film on an aluminum brazing sheet during heating.

### **Paper I: The thickness of native oxides on aluminum alloys and single crystals**

In this paper the native oxide thickness of two pure aluminum single crystals, a nickel aluminum single crystal, and four different industrial standard aluminum alloys was determined and the differences between the samples were discussed. To obtain a solid understanding of the thickness three experimental techniques were used.

The oxide thickness can be deduced in XPS from the fitted intensities of the oxide and the metallic peak in the Al spectrum. By using the intensities, the tabulated volume densities for aluminum and aluminum oxide as well as the IMFP for both layers, the thickness can be approximated according to formula (1) in paper I. Calculating the thickness according to this model which assumes a pure oxide and metal layer will be more descriptive of an aluminum single crystal than of an alloy since it does not take into account the variation in the IMFP and volume density by the presence of alloying elements.

The thickness obtained from XRR are directly derived from the fits of the reflectivity curve. Here a multilayer model was fitted that assigns every layer with a certain thickness and electron density. Since the initial parameters are optimized during the fitting procedure the thickness obtained by XRR are not sensitive to differences in the composition as in XPS.

In EIS the oxide layer modeled as a parallel plate capacitor which has a specific dielectric constant related to the structure and composition of the oxide. Since the same value for the dielectric constant was used for all samples, the calculated thickness is more reliable for the single crystals than for the alloys.

All three techniques indicate that the native oxide layer is thicker on aluminum alloys than on the single crystals. The increased thickness for the alloyed samples

can be explained first of all by the grain structure. The single crystals have no grain boundaries that can act as fast transfer sites for ions and therefore they have a smaller mass transfer rate than the polycrystalline samples. Another aspect is the presence of alloying elements which exhibit different chemical reactivities and disrupt the continuous oxide film.

## **Paper II: Surface development of an aluminum brazing sheet during heating studied by XPEEM and XPS**

A combination of microscopy and spectroscopy techniques was used in this paper to follow the surface development of an aluminum brazing sheet during heating up to the melting temperature. To trace the chemical changes on the surface is of great interest since the surface determines how well two work pieces can be joined by brazing.

The chemical changes were studied with XPEEM for the three main elements in the braze cladding Al, Si, and Mg. The images were taken at a FOV of  $50\mu\text{m}$  to have a maximum overview of the sample. To allow the generation of XP spectra of certain areas within the XPEEM images, they were obtained in stacks, meaning that over a range of binding energies, here 10 eV, an image is taken after a small energy step, here 0.25 eV. XPEEM stacks are particularly useful for inhomogeneous samples like alloys since it makes it possible to follow local chemical changes of different particles or phases simultaneously, as shown in paper II Fig. 6. To understand how the sample is changing in average, conventional XPS measurements were performed for Al 2p, Si 2p, Mg 2p, and O 1s core-levels. Complementary to the chemical information the sample's topography was studied with MEM/LEEM. Additionally, SEM images were taken *ex-situ* to image the sample's topography after reoxidizing in air.

Using the different techniques mixed Al and Si-rich particles were identified as well as the formation of  $\text{MgAl}_2\text{O}_4$ -rich areas at  $540^\circ\text{C}$ . Further, micrometer large metallic Mg particles segregated to the surface at  $560^\circ\text{C}$ . At the same temperature the surface changes from being rich in Al and Si oxides to a mainly metallic surface without silicon. By increasing the temperature to  $580^\circ\text{C}$  magnesium evaporates leaving a metallic aluminum surface behind. A sketch summarizing the chemical changes can be found in paper II Fig. 10. This shows how the heterogeneous surface is being transformed from an oxide to a metallic surface by the diffusion of Mg and how locally new  $\text{MgAl}_2\text{O}_4$  phases are formed.

## 5 Outlook

Papers I and II show how methods typical for surface science can be applied to industrial type samples. First attempts of recreating an industrial environment were undertaken in paper I by measuring the oxide thickness in water and in paper II by heating up to brazing temperatures.

To create more realistic sample environments Ambient Pressure XPS (APXPS) measurement are planned. APXPS makes it possible to study the oxide decomposition on brazing alloys in pressures and temperatures that are similar to the ones used in brazing furnaces. This will provide information on the chemical changes at the surface. By using different gas mixture it will be feasible to compare vacuum brazing (pressures lower than  $10^{-5}$  mbar) to brazing in protective atmospheres, e.g. several mbars of nitrogen.

Unfortunately, no environmental XPEEM has been fully developed even though first attempts have been made [50,62]. However, XPEEM and LEEM measurements can be performed with video-rate frequency which will enable real-time monitoring of surface processes. To compensate for the thermal drift that is occurring during heating experiments, plans of patterning samples with focused ion beam lithography (FIB) have been made. This will allow an easy recognition of the different areas on the sample.

XRR measurements can also be conducted in wet environments. This will allow for corrosion testing in different kinds of salt solutions or acids. Even though only the thickness of different layers can be determined, very substantial understanding about when the protective oxide layer is broken down or how a especially thick oxide layer can be grown by anodization can be obtained.

To explore the full range of possibilities that open up with more industrial like sample environments, plans of investigating other types of materials have been made. First experiments have been conducted on super duplex stainless steels like SAF 2507. These samples are even more of a challenge because of their two phases, austenite and ferrite, that also have different crystal structures and composition. Here, diffraction based techniques like LEED, LEEM, and X-ray diffraction (XRD) will be useful for identifying structural changes.

The general trend for material science experiments with surface science techniques is to move towards industrial samples which will be than characterized in environments that mimic the industrial process. Therefore it will be the main challenge to handle more and more complex experimental set-ups and the difficulties arising from data sets that depend on an increasing number of variables.



# References

- [1] R. Lumley. *Fundamentals of aluminium metallurgy : production, processing and applications*. Cambridge : Woodhead Publishing Limited, 2010. doi:10.1533/9780857090256.
- [2] P. Roberts. *Industrial Brazing Practice, Second Edition*. CRC Press, 2013. doi:10.1201/b14061.
- [3] C. McConville, D. Seymour, D. Woodruff and S. Bao. “Synchrotron radiation core level photoemission investigation of the initial stages of oxidation of Al(111)”. *Surface Science*, 188(1-2), 1–14, 1987. doi:10.1016/s0039-6028(87)80138-3.
- [4] H. Brune, J. Winterlin, R. J. Behm and G. Ertl. “Surface migration of “hot” adatoms in the course of dissociative chemisorption of oxygen on Al(111)”. *Physical Review Letters*, 68(5), 624–626, 1992. doi:10.1103/physrevlett.68.624.
- [5] C. Berg, S. Raaen, A. Borg, J. N. Andersen, E. Lundgren and R. Nyholm. “Observation of a low-binding-energy peak in the 2pcore-level photoemission from oxidized Al(111)”. *Physical Review B*, 47(19), 13063–13066, 1993. doi:10.1103/physrevb.47.13063.
- [6] L. Jeurgens, W. Sloof, F. Tichelaar, C. Borsboom and E. Mittemeijer. “Determination of thickness and composition of aluminium-oxide overlayers on aluminium substrates”. *Applied Surface Science*, 144-145, 11–15, 1999. doi:10.1016/s0169-4332(98)00755-7.
- [7] P. Snijders, L. Jeurgens and W. Sloof. “Structure of thin aluminium-oxide films determined from valence band spectra measured using XPS”. *Surface Science*, 496(1-2), 97–109, 2002. ISSN 0039-6028. doi:http://dx.doi.org/10.1016/S0039-6028(01)01591-6.

- [8] N. Cai, G. Zhou, K. Müller and D. E. Starr. “Effect of oxygen gas pressure on the kinetics of alumina film growth during the oxidation of Al(111) at room temperature”. *Physical Review B*, 84(12), 2011. doi:10.1103/physrevb.84.125445.
- [9] E. Lundgren. “SSF Program ALUminium oXides for processing and products ALUX”. web, 2017.
- [10] M. Schmid, G. Leonardelli, R. Tscheließnig, A. Biedermann and P. Varga. “Oxygen adsorption on Al(111): low transient mobility”. *Surface Science*, 478(3), L355–L362, 2001. doi:10.1016/s0039-6028(01)00967-0.
- [11] D. Starodub, T. Gustafsson and E. Garfunkel. “The reaction of  $O_2$  with Al(110): a medium energy ion scattering study of nano-scale oxidation”. *Surface Science*, 552(1-3), 199–214, 2004. doi:10.1016/j.susc.2004.01.019.
- [12] W. Hosford. *Physical Metallurgy, Second Edition*. Informa UK Limited, 2010. doi:10.1201/b15858.
- [13] A. N. Adamson, E. J. Bloore and A. R. Carr. “Basic Principles of Bayer Process Design”. In “Essential Readings in Light Metals”, pages 100–117. Wiley-Blackwell, 2013. doi:10.1002/9781118647868.ch14.
- [14] W. E. Haupin. “Principles of Aluminum Electrolysis”. In “Essential Readings in Light Metals”, pages 3–11. Springer Nature, 2016. doi:10.1007/978-3-319-48156-2\_1.
- [15] D. V. Schroeder. *An Introduction to Thermal Physics*. Addison Wesley Pub Co Inc, 1999. ISBN 0201380277. doi:https://doi.org/10.1016/B978-0-12-803304-3.09981-6.
- [16] I. Levin and D. Brandon. “Metastable Alumina Polymorphs: Crystal Structures and Transition Sequences”. *Journal of the American Ceramic Society*, 81(8), 1995–2012, 2005. doi:10.1111/j.1151-2916.1998.tb02581.x.
- [17] “Sapphire ( $Al_2O_3$ -rhom) Crystal Structure: Datasheet from “PAULING FILE Multinaries Edition – 2012” in SpringerMaterials”.
- [18] K. Momma and F. Izumi. “VESTA 3for three-dimensional visualization of crystal, volumetric and morphology data”. *Journal of Applied Crystallography*, 44(6), 1272–1276, 2011. doi:10.1107/s0021889811038970.
- [19] E. Balan, M. Lazzeri, G. Morin and F. Mauri. “First-principles study of the OH-stretching modes of gibbsite”. *American Mineralogist*, 91(1), 115–119, 2006. doi:10.2138/am.2006.1922.

- [20] G. Kresse. “Structure of the Ultrathin Aluminum Oxide Film on NiAl(110)”. *Science*, 308(5727), 1440–1442, 2005. doi:10.1126/science.1107783.
- [21] N. M. Martin, J. Knudsen, S. Blomberg, J. Gustafson, J. N. Andersen, E. Lundgren, H. H. Ingelsten, P.-A. Carlsson, M. Skoglundh, A. Stierle and G. Kresse. “High-resolution core-level spectroscopy study of the ultrathin aluminum oxide film on NiAl(110)”. *Physical Review B*, 83(12), 2011. doi:10.1103/physrevb.83.125417.
- [22] G. Prévot, S. L. Moal, R. Bernard, B. Croset, R. Lazzari and D. Schmaus. “Archetypal structure of ultrathin alumina films: Grazing-incidence x-ray diffraction on Ni(111)”. *Physical Review B*, 85(20), 2012. doi:10.1103/physrevb.85.205450.
- [23] G. Prévot, A. Naitabdi, R. Bernard and Y. Borensztein. “Sixton rectangles in the structure of alumina ultrathin films on metals”. *Physical Review B*, 81(8), 2010. doi:10.1103/physrevb.81.085405.
- [24] L. Jeurgens, W. Sloof, F. Tichelaar and E. Mittemeijer. “Thermodynamic stability of amorphous oxide films on metals: Application to aluminum oxide films on aluminum substrates”. *Physical Review B*, 62(7), 4707–4719, 2000. doi:10.1103/physrevb.62.4707.
- [25] C. Vargel. “Physical Properties of Aluminium”. In “Corrosion of Aluminium”, pages 19–20. Elsevier BV, 2004. doi:10.1016/b978-008044495-6/50007-0.
- [26] B. McGurran and M. Nicholas. “A study of aluminium brazes using hot-stage scanning electron microscopy”. *Journal of Materials Science*, 19(8), 2713–2718, 1984. ISSN 0022-2461. doi:10.1007/BF00550829.
- [27] D. K. Creber, J. Ball and D. J. Field. “A Mechanistic Study of Aluminum Vacuum Brazing”. In “SAE Technical Paper”, SAE International, 1987. doi:10.4271/870185.
- [28] L. Rullik, F. Bertram, Y. R. Niu, J. Evertsson, T. Stenqvist, A. A. Zakharov, A. Mikkelsen and E. Lundgren. “Surface development of an aluminum brazing sheet during heating studied by XPEEM and XPS”. *Materials Research Express*, 3(10), 106506, 2016. doi:10.1088/2053-1591/3/10/106506.
- [29] F. Goodwin, S. Guruswamy, K. U. Kainer, C. Kammer, W. Knabl, A. Koethe, G. Leichtfried, G. Schlamp, R. Stickler and H. Warlimont. *Metals*,

- pages 161–430. Springer Berlin Heidelberg, Berlin, Heidelberg, 2005. ISBN 978-3-540-30437-1. doi:10.1007/3-540-30437-1.5.
- [30] F. Zhang, J.-O. Nilsson and J. Pan. “In Situ and Operando AFM and EIS Studies of Anodization of Al 6060: Influence of Intermetallic Particles”. *Journal of The Electrochemical Society*, 163(9), C609–C618, 2016. doi:10.1149/2.0061610jes.
- [31] F. Bertram, F. Zhang, J. Evertsson, F. Carlà, J. Pan, M. E. Messing, A. Mikkelsen, J.-O. Nilsson and E. Lundgren. “In situ anodization of aluminum surfaces studied by x-ray reflectivity and electrochemical impedance spectroscopy”. *Journal of Applied Physics*, 116(3), 034902, 2014. doi:10.1063/1.4890318.
- [32] J. Evertsson, F. Bertram, F. Zhang, L. Rullik, L. Merte, M. Shipilin, M. Soldemo, S. Ahmadi, N. Vinogradov, F. Carlà, J. Weissenrieder, M. Göthelid, J. Pan, A. Mikkelsen, J.-O. Nilsson and E. Lundgren. “The thickness of native oxides on aluminum alloys and single crystals”. *Applied Surface Science*, 349, 826–832, 2015. doi:10.1016/j.apsusc.2015.05.043.
- [33] J. D. Jackson. *Classical electrodynamics*. New York : Wiley, 1999.
- [34] A. Liénard. “Champ Électrique et Magnétique”. *L’Éclairage Électrique*, 16, 5–14, 53–59, 106–112, 1898.
- [35] A. Hofmann. *The Physics of Synchrotron Radiation*. Cambridge University Press, 2004.
- [36] K. Wille. *The physics of particle accelerators : an introduction*. Oxford : Oxford University Press, 2000.
- [37] J. Als-Nielsen and D. McMorrow. “Refraction and reflection from interfaces”. In “Elements of Modern X-ray Physics”, pages 69–112. Wiley-Blackwell, 2011. doi:10.1002/9781119998365.ch3.
- [38] H. Hertz. “Über einen Einfluss des ultravioletten Lichtes auf die elektrische Entladung”. *Annalen der Physik*, 267(8), 983–1000, 1887. doi:10.1002/andp.18872670827.
- [39] A. Einstein. “Über einen die Erzeugung und Verwandlung des Lichtes betreffenden heuristischen Gesichtspunkt”. *Annalen der Physik*, 322(6), 132–148, 1905. doi:10.1002/andp.19053220607.
- [40] “[http://www.nobelprize.org/nobel\\_prizes/physics/laureates/1921/](http://www.nobelprize.org/nobel_prizes/physics/laureates/1921/)”. Web, 13 Feb 2014. The Nobel Prize in Physics 1921, Nobel Media AB.

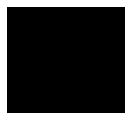
- [41] K. Siegbahn. “Electron Spectroscopy for Atoms, Molecules, and Condensed Matter”. *Science*, 217(4555), 111–121, 1982. doi:10.1126/science.217.4555.111.
- [42] “[http://www.nobelprize.org/nobel\\_prizes/physics/laureates/1981/](http://www.nobelprize.org/nobel_prizes/physics/laureates/1981/)”. Web, 13 Feb 2014. The Nobel Prize in Physics 1981, Nobel Media AB.
- [43] S. Tanuma, C. J. Powell and D. R. Penn. “Calculations of electron inelastic mean free paths”. *Surface and Interface Analysis*, 37(1), 1–14, 2005. doi:10.1002/sia.1997.
- [44] S. Hüfner. *Photoelectron spectroscopy : principles and applications*. Advanced texts in physics. Berlin : Springer, 2003. doi:10.1007/978-3-662-09280-4.
- [45] V. Schmidt. “Photoionization of atoms using synchrotron radiation”. *Reports on Progress in Physics*, 55(9), 1483–1659, 1992. doi:10.1088/0034-4885/55/9/003.
- [46] M. Grioni. *Photoelectron Spectroscopy*, pages 189–237. Springer Netherlands, Dordrecht, 2006. ISBN 978-1-4020-3337-7. doi:10.1007/1-4020-3337-0\_6.
- [47] Y. Joly and S. Grenier. *Theory of X-Ray Absorption Near Edge Structure*, pages 73–97. John Wiley & Sons, Ltd, 2016. ISBN 9781118844243. doi:10.1002/9781118844243.ch4.
- [48] C. S. Schnohr and M. C. Ridgway (Editors). *X-Ray Absorption Spectroscopy of Semiconductors*. Springer Berlin Heidelberg, 2015. doi:10.1007/978-3-662-44362-0.
- [49] O. H. Griffith and W. Engel. “Historical perspective and current trends in emission microscopy, mirror electron microscopy and low-energy electron microscopy”. *Ultramicroscopy*, 36(1-3), 1–28, 1991. doi:10.1016/0304-3991(91)90135-s.
- [50] “<http://www.elmitec-gmbh.com/>”. Web, 19 Mar 2014. ELMITEC Elektronenmikroskopie GmbH.
- [51] E. Bauer. *Surface Microscopy with Low Energy Electrons*. Springer New York, 2014.
- [52] W. Świech, B. Rausenberger, W. Engel, A. Bradshaw and E. Zeitler. “In-situ studies of heterogeneous reactions using mirror electron microscopy”. *Surface Science*, 294(3), 297–307, 1993. doi:10.1016/0039-6028(93)90116-2.

- [53] G. F. Rempfer and O. H. Griffith. “Emission microscopy and related techniques: Resolution in photoelectron microscopy, low energy electron microscopy and mirror electron microscopy”. *Ultramicroscopy*, 47, 35–54, 1992. doi:10.1016/0304-3991(92)90184-L.
- [54] S. M. Kennedy, D. E. Jesson and D. M. Paganin. “Laplacian and caustic imaging theories of MEM work-function contrast”. *IBM Journal of Research and Development*, 55(4), 3:1–3:8, 2011. doi:10.1147/jrd.2011.2143310.
- [55] C. Schneider. *Soft X-ray photoelectron emission-microscopy (X-PEEM)*. Springer Netherlands, 2006. doi:10.1007/1-4020-3337-0-8.
- [56] J. Stohr and S. Anders. “X-ray spectro-microscopy of complex materials and surfaces”. *IBM Journal of Research and Development*, 44(4), 535–551, 2000. doi:10.1147/rd.444.0535.
- [57] R. Tromp, J. Hannon, W. Wan, A. Berghaus and O. Schaff. “A new aberration-corrected, energy-filtered LEEM/PEEM instrument II. Operation and results”. *Ultramicroscopy*, 127, 25–39, 2013. doi:10.1016/j.ultramic.2012.07.016.
- [58] R. Nyholm, J. Andersen, U. Johansson, B. Jensen and I. Lindau. *Nuclear Instruments and Methods in Physics Research Section A: Accelerators, Spectrometers, Detectors and Associated Equipment*, 467 - 468, Part 1, 520 – 524, 2001. doi:10.1016/S0168-9002(01)00399-0.
- [59] J. Feng and A. Scholl. *Photoemission Electron Microscopy (PEEM)*. New York: Springer, 2007. doi:10.1007/978-0-387-49762-4\_9.
- [60] E. Bauer. “A brief history of PEEM”. *Journal of Electron Spectroscopy and Related Phenomena*, 185(10), 314–322, 2012. doi:10.1016/j.elspec.2012.08.001.
- [61] E. B. A Locatelli. “Recent advances in chemical and magnetic imaging of surfaces and interfaces by XPEEM”. *Journal of Physics: Condensed Matter*, 20(9), 093002, 2008. doi:10.1088/0953-8984/20/9/093002.
- [62] H. Guo, E. Strelcov, A. Yulaev, J. Wang, N. Appathurai, S. Urquhart, J. Vinson, S. Sahu, M. Zwolak and A. Kolmakov. “Enabling Photoemission Electron Microscopy in Liquids via Graphene-Capped Microchannel Arrays”. *Nano Letters*, 17(2), 1034–1041, 2017. doi:10.1021/acs.nanolett.6b04460.

# Scientific publications



Paper I







## The thickness of native oxides on aluminum alloys and single crystals

J. Evertsson<sup>a,\*</sup>, F. Bertram<sup>a</sup>, F. Zhang<sup>c</sup>, L. Rullik<sup>a</sup>, L.R. Merte<sup>a</sup>, M. Shipilin<sup>a</sup>, M. Soldemo<sup>e</sup>,  
S. Ahmadi<sup>e</sup>, N. Vinogradov<sup>d</sup>, F. Carlà<sup>d</sup>, J. Weissenrieder<sup>e</sup>, M. Göthelid<sup>e</sup>, J. Pan<sup>c</sup>,  
A. Mikkelsen<sup>a</sup>, J.-O. Nilsson<sup>b</sup>, E. Lundgren<sup>a</sup>

<sup>a</sup> Division of Synchrotron Radiation Research, Lund University, Box 118, 221 00 Lund, Sweden

<sup>b</sup> Sapa Technology, Kanalгатan 1, 612 31 Finspång, Sweden

<sup>c</sup> KTH Royal Institute of Technology, Department of Chemistry, Division of Surface and Corrosion Science, Drottning Kristinas Vg 51, 100 44 Stockholm, Sweden

<sup>d</sup> ESRF, B.P. 220, 38043 Grenoble, France

<sup>e</sup> KTH Royal Institute of Technology, ICT, Material Physics, 16440 Kista, Sweden

### ARTICLE INFO

#### Article history:

Received 8 January 2015

Received in revised form 22 April 2015

Accepted 8 May 2015

Available online 16 May 2015

#### Keywords:

Aluminum alloy

Aluminum single crystal

Thin native oxide film thickness

Electrochemical impedance spectroscopy

X-ray reflectivity

X-ray photoelectron spectroscopy

### ABSTRACT

We present results from measurements of the native oxide film thickness on four different industrial aluminum alloys and three different aluminum single crystals. The thicknesses were determined using X-ray reflectivity, X-ray photoelectron spectroscopy, and electrochemical impedance spectroscopy. In addition, atomic force microscopy was used for micro-structural studies of the oxide surfaces. The reflectivity measurements were performed in ultra-high vacuum, vacuum, ambient, nitrogen and liquid water conditions. The results obtained using X-ray reflectivity and X-ray photoelectron spectroscopy demonstrate good agreement. However, the oxide thicknesses determined from the electrochemical impedance spectroscopy show a larger discrepancy from the above two methods. In the present contribution the reasons for this discrepancy are discussed. We also address the effect of the substrate type and the presence of water on the resultant oxide thickness.

© 2015 Elsevier B.V. All rights reserved.

### 1. Introduction

Aluminum and its alloys are commonly used in everyday products and are of interest for applications such as corrosion protection, microelectronics and thermal barriers. For many of these applications, the amorphous native aluminum oxide film which is formed spontaneously at ambient pressures and at low temperatures dictates the properties of functional aluminum [1,2]. For example, the corrosion protection properties of aluminum can be related to the properties of this film as it prevents further oxidation and is self-renewing in case of mechanical damage in ambient and in aqueous conditions [3].

The growth of oxide films on metals at ambient pressures and low temperatures has been addressed in detail by Cabrera and Mott [1,2]. In their model, electrons from the metal traverse the growing oxide, forming anions with the oxygen on the surface. The negative oxygen anions and the positive metallic cations below the oxide create a so-called Mott potential. The Mott potential

decreases the barrier for migration of oxygen anions and/or metallic cations through the oxide. Consequently, the growth rate increases and is extremely rapid initially [1]. Nevertheless, with increasing thickness of the oxide, the additional effect of the Mott potential decreases and when the effect is too small to significantly affect the ion transport, the oxide growth stops and a limiting thickness is reached. This theory explains the process and estimates the limiting thickness well, but recent theoretical calculations have shown that a real limiting thickness is likely to also be defined by the reduced oxygen adsorption energy upon oxide layer formation [4].

Due to the many attractive properties of aluminum and its oxides, much research, both fundamental and applied, has been performed for decades. Surface science studies, both theoretical and experimental, have provided fundamental information on the initial stages of the formation of the oxide [4–14]. Whereas the exact atomic scale structure of ultrathin aluminum oxides is known from a limited number of studies [15–17], the detailed atomic arrangement in aluminum oxides for applications has been detained due to its complex structure. Further, most studies have been performed using electron-based methods. Because of the short electron inelastic mean free path, these studies have been limited to highly controlled ultra-high vacuum (UHV) conditions.

\* Corresponding author. Tel.: +46 46 2220469.

E-mail address: [jonas.evertsson@sljus.lu.se](mailto:jonas.evertsson@sljus.lu.se) (J. Evertsson).

This is far from the realistic conditions where the industrial aluminum products need to perform, i.e. ambient air pressure and high humidity or even aqueous environments. In addition, the industrial polycrystalline aluminum products used today contain certain amounts of alloying elements such as Mg, Si, Fe and Zn. These alloying elements are primarily introduced in order to improve the mechanical properties of Al-based products, as well as enhance their oxidation resistance. However, the presence of these elements, further complicates fundamental studies of the oxidation process for these alloys.

Aluminum alloys have long been studied using electrochemical methods in aqueous environments, for example by electrochemical impedance spectroscopy (EIS) [18]. This has for instance provided information on the properties of the oxide, such as the effect of the alloying elements on the corrosion protection and the thickness of the oxide film.

Since electron-based methods fail in more realistic conditions, methods based on hard X-rays, that have a much longer penetration depth, allow for surface studies in ambient pressures as well as under aqueous conditions [19,20,20]. Combining electrochemical methods and hard X-ray methods could be an important approach to increase the understanding of complex aluminum alloys and their oxides under more realistic conditions.

In the present article, we report a study of the thickness of the native oxide films, hereafter referred to as oxides, on three different aluminum single crystals [NiAl(1 1 0), Al(1 0 0) and Al(1 1 1)] and four different industrial aluminum alloys [AA 6005A, AA 6060, AA 6063 and AA 7075] determined using X-ray reflectivity (XRR), EIS and X-ray photoelectron spectroscopy (XPS). The primary aim of this study is to compare the oxide thicknesses obtained by different techniques in different sample environments. The results show that the determined thicknesses vary depending on the technique applied and the sample environment. Secondly, this contribution addresses the effect of substrate on the oxide thicknesses. This is based on comparison of oxide thicknesses on Al single crystals, Al alloys and between Al alloys individually. Finally we discuss briefly how the history of the sample may affect the resulting oxide thickness.

## 2. Experimental

We studied the oxide thickness on three different single crystals and four different industrial Al alloys. Table 1 shows the sample compositions. The NiAl(1 1 0), Al(1 0 0) and Al(1 1 1) single crystals were purchased from Surface Preparation Laboratory (SPL), Zaandam, The Netherlands. The AA 6005A, AA 6060, AA 6063 and AA 7075 alloys were cut from extruded Al profile products from Sapa Technology, Finspång, Sweden. The alloys and the single crystals were polished to mirror-finish by SPL. During the polishing the old passive oxide film is removed with a subsequent natural growth of a new passive film. We assume that at the time for the measurements, the oxide have reached the limiting thickness as described by the Cabrera–Mott model. Possible additional oxide growth is not directly controlled. However, no larger changes are obvious in the XRR obtained thicknesses although the XRR measurements were performed at several occasions during a time span of one year.

For the determination of the oxide thicknesses three methods were used; XRR, EIS and XPS. For surface structure studies, atomic force microscopy (AFM) was also used.

The XRR measurements were performed in four different setups in five different environments. Measurements in ambient conditions were performed when the sample were not enclosed in a cell (hereafter referred to as without cell). Measurements in atmospheric pressures of nitrogen, ambient and ultrapure liquid water (hereafter referred to as water) conditions were performed using a cell with PEEK walls, described by Foresti et al. [23]. Measurements

in UHV and  $10^{-5}$  bar (hereafter referred as vacuum) were performed using a batch cell with beryllium walls described by Bernard et al. [24] and an Anton Parr DHS1100 cell [25] with graphite walls, respectively. Three different photon energies were used; 10 keV at the Petra III/DESY beamline P08 [26] and either 18 keV or 24 keV at the ESRF beamline ID03 [27].

The XPS experiments were carried out in UHV at the beamline I311, Max IV [28] using a photon energy of 650 eV.

The EIS spectra were recorded using a three-electrode setup with a Multi Autolab instrument. In the setup a saturated Ag/AgCl electrode, inside a Luggin capillary, was used as reference electrode, the sample with an exposed area of  $0.3\text{ cm}^2$  was used as working electrode and a Pt mesh was used as counter electrode. A 2 M  $\text{Na}_2\text{SO}_4$  solution was used as electrolyte and the measurements were recorded after reaching a stable open circuit potential (OCP). The solution is a near neutral electrolyte, which enables EIS measurements at the same time as the corrosion rate is low. The EIS spectra were collected and analyzed using the Nova software 1.9.

## 3. Results

### 3.1. X-ray reflectivity (XRR)

For comparison of the oxide thicknesses of six different samples [Al(1 0 0), Al(1 1 1), AA 6005A, AA 6060, AA 6063 and AA 7075], XRR measurements were performed in ambient conditions without cell. The XRR measurements are performed by measuring the reflected X-ray beam intensity as function of the incidence angle to the sample surface. The results are shown in Fig. 1, where the intensity is presented as a function of X-ray scattering vector. Experimental (blue dots) and fitted (red line) data of the XRR measurements are shown in Fig. 1(a).

The intensity oscillations originate from the interference of reflected beams from the interfaces of different layers of the sample. Hence, from the period of the oscillation the oxide thickness can be determined, where a shorter period indicates a thicker oxide. To obtain a quantitative estimation of the thickness, the data were fitted using the Parratt-algorithm [29] with a Névo-Corcor roughness model [30]. The Parratt algorithm is a recursive algorithm that uses Fresnel reflectivity of each interface in a multilayer model where each layer is characterized by a certain thickness and electron density. The Névo-Corcor model takes into account the roughness damping assuming an error-function profile for the electron density. The thicknesses determined from the fits are shown in Fig. 1(b).

The difference in the oscillation period observed for different samples implies different oxide thicknesses. The oxide thicknesses on the industrial alloys are generally higher than on the single crystals, especially the oxide on AA 6005A and AA 7075 alloys are notably thicker (~50–100%).

XRR experiments were also performed to compare how a water environment affects the film thickness for oxides grown in ambient conditions. For this two XRR measurements of the same sample were performed in a cell with PEEK walls, first in nitrogen and then after filling the cell with water. The same sample is used for the measurements in both environments to avoid having samples of the same type, but with different oxide thicknesses. Fig. 2(a) shows the result from the experiment performed on three different samples [NiAl(1 1 0), Al(1 1 1) and AA 6060]. The shorter oscillation period for all measurements in water indicates that the oxides are thicker in water than in nitrogen. The thicknesses have also been determined by fitting, see Fig. 2(b).

### 3.2. X-ray photoelectron spectroscopy (XPS)

For comparison with the XRR results also XPS experiments of four different samples [Al(1 0 0), Al(1 1 1), AA 6063 and AA 7075]

**Table 1**  
Aluminum sample compositions [wt.%) [22].

Sample	Si	Fe	Cu	Mn	Mg	Cr	Zn	Ti	Ni	Al
NiAl(110)	0	0	0	0	0	0	0	0	50	50
Al(100)	0	0	0	0	0	0	0	0	0	100
Al(111)	0	0	0	0	0	0	0	0	0	100
AA 6005A	0.50–0.90	0.35	0.30	0.50	0.40–0.70	0.30	0.20	0.10	0	Remainder
AA 6060	0.30–0.60	0.10–0.30	0.10	0.10	0.35–0.60	0.05	0.15	0.10	0	Remainder
AA 6063	0.20–0.60	0.35	0.10	0.10	0.45–0.90	0.10	0.10	0.10	0	Remainder
AA 7075	0.40	0.50	1.2–2.0	0.30	2.1–2.9	0.18–0.28	5.1–6.1	0.20	0	Remainder

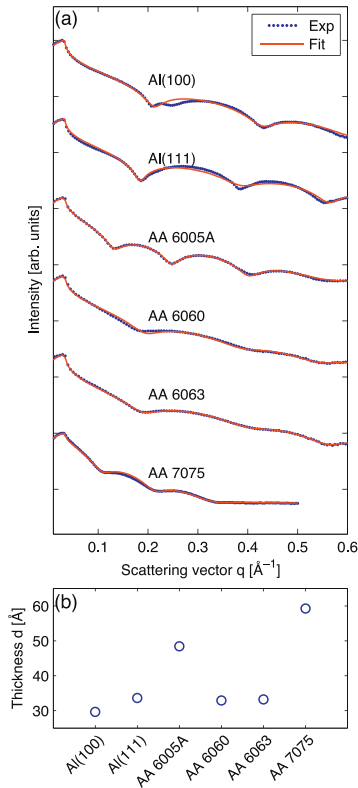


**Fig. 1.** Experimental data and fits of the XRR measurements of the oxide on different industrial Al alloys and single crystal surfaces performed in ambient conditions without cell (a). The blue dots correspond to the experimental data and the red lines correspond to the fits. The thicknesses obtained from the fits are shown in (b). (For interpretation of the references to color in this figure legend, the reader is referred to the web version of the article.)

were performed. Fig. 3(a)–(d) shows the XPS spectra of the Al 2p peaks of the AA 6063, AA 7075, Al(111) and Al(100) samples, respectively. To determine the thickness, the samples were modeled as a homogenous oxide layer on top of a homogenous Al substrate. From such a system the oxide thickness is possible to determine using the equation [31]:

$$d_{XPS} = \lambda_{ox} \sin \Theta \ln \left( \frac{N_{me} \lambda_{me} I_{ox}}{N_{ox} \lambda_{ox} I_{me}} + 1 \right) \quad (1)$$

For all thickness determinations, shown in Fig. 3(e), the same values, except for the intensities  $I_{ox}$  and  $I_{me}$ , in the equation for the oxide and Al were used. The ratio of the volume densities of Al atoms in metal to oxide  $N_{me}/N_{ox} = 1.6$ , calculated using the densities  $2.7 \text{ g cm}^{-3}$  and  $3.1 \text{ g cm}^{-3}$  for the Al and oxide, respectively. The electron inelastic mean free path (IMFP) in the metal and the oxide,  $\lambda_{ox} = 16.8 \text{ \AA}$  and  $\lambda_{me} = 15.5 \text{ \AA}$ , calculated for a kinetic energy of 575 eV using the software QUASES-IMFP-TPP2M [32], which uses

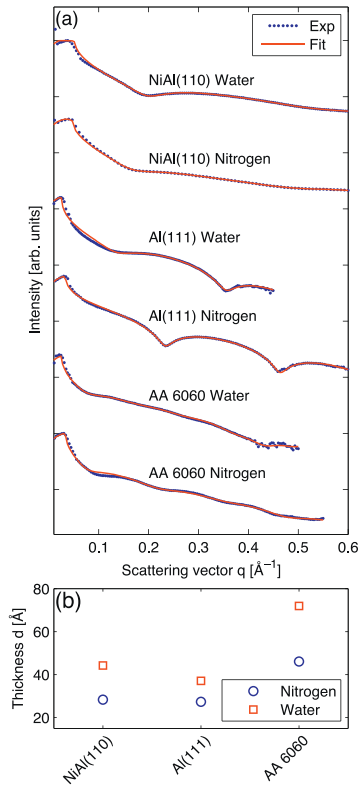


**Fig. 2.** Experimental data and fits of the XRR measurements of the oxide on different industrial Al alloys and single crystal surfaces performed in nitrogen and water using a PEEK cell (a). The blue dots correspond to the experimental data and the red lines correspond to the fits. The thicknesses obtained from the fits are shown in (b), where blue circles and red squares indicate the thickness in nitrogen and water, respectively. (For interpretation of the references to color in this figure legend, the reader is referred to the web version of the article.)

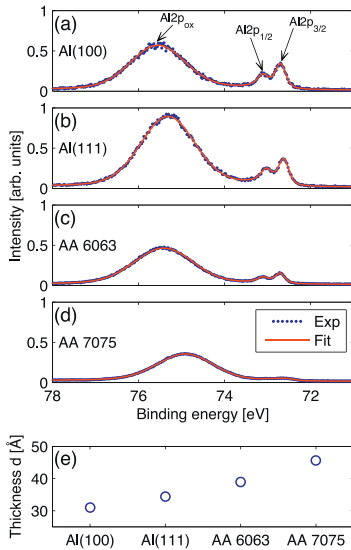


**Fig. 3.** XPS measurements from (a) the Al(1 0 0), (b) the Al(1 1 1), (c) the AA 6063 and (d) the AA 7075 sample obtained in UHV using a photon energy of 650 eV. The blue dots corresponds to the experimental data and the red lines corresponds to the fits. The spectra in (a–d) are fitted using one peak Al 2p<sub>ox</sub> for the oxidized and two Al 2p<sub>3/2</sub> and Al 2p<sub>1/2</sub> peaks for the metallic contribution, respectively. More intense metallic peaks indicate a thinner oxide. The thicknesses determined using the ratio between the area of the oxidized and metallic Al 2p contributions and assuming the same properties of the oxide and the metal for all samples are shown in (e).

the TPP2M formula from Ref. [33]. The photoelectron emission angle was  $\theta = 90^\circ$ . The intensities,  $I_{ox}$  and  $I_{me}$ , were obtained by fitting one peak to the oxide component (Al 2p<sub>ox</sub>) and the two peaks (Al 2p<sub>3/2</sub>, 1/2) to the metallic component as shown in (a). The results show that the oxides are thicker on the industrial alloys than on the single crystals.

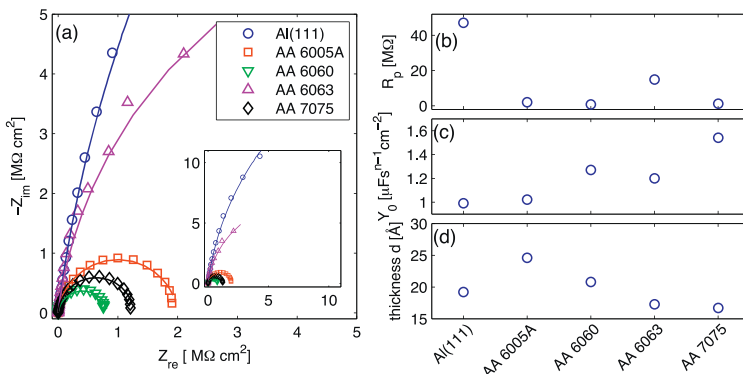


**Fig. 4.** EIS measurements. Recorded data and fits (lines) represented in a Nyquist plot is shown in (a). The  $R_p$  and  $Y_0$  values obtained from fitting the circuit in Fig. 5 to the recorded data is shown in (b) and (c), respectively. The thicknesses calculated from the capacitance assuming a parallel-plate capacitor like behavior of the oxide are shown in (d).

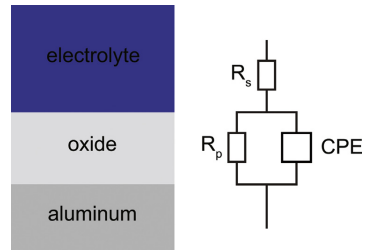


**Fig. 5.** Sketch of the equivalent circuit describing the metal–electrolyte interface, where the electrolyte is represented by the solution resistance ( $R_s$ ) and the oxide as a polarization resistance ( $R_p$ ) together with a constant phase element (CPE) in parallel.

3.3. Electrochemical impedance spectroscopy (EIS)

EIS measurements were performed for comparison with the XRR and the XPS results. A measurement is performed by applying perturbation potentials to the electrochemical system with different frequencies and measuring the response current. In our measurements the potential had an amplitude of 10 mV and frequencies between  $10^{-2}$  and  $10^4$  Hz. The results for five different samples [Al(1 1 1), AA 6005A, AA 6060, AA 6063, and AA 7075] are shown in Fig. 4. The recorded data represented in a Nyquist plot are shown in Fig. 4(a). The Nyquist plot shows the real  $Z_{re}$  and imaginary  $Z_{im}$  parts of the impedance, where each point corresponds to one frequency. The impedance is the ratio between the applied potential and the response current.

The data from each measurement show essentially one time constant feature. The oxide can therefore be modelled as a single homogenous layer described by the simple equivalent circuit shown in Fig. 5. In the model the electrolyte is represented by the solution resistance ( $R_s$ ) and the oxide as a polarization resistance ( $R_p$ ) together with a constant phase element (CPE) in parallel. The CPE element is used instead of a pure capacitor, since the capacitance response of the oxide is not ideal. The CPE impedance function  $Z_{CPE}(\omega) = 1/Y_0(j\omega)^n$ . From the values  $Y_0$ ,  $n$  and  $R_p$  [34] obtained from fitting of the data using the model, it is possible to derive the systems capacitance  $C = (Y_0 R_p)^{1/n} / R_p$ . The  $R_p$  and  $Y_0$  values obtained

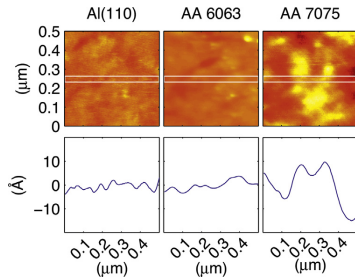


**Fig. 6.** AFM images of Al(1 1 0), AA 6063 and AA 7075 with corresponding line profiles below each image showing the roughness of the sample. The line profiles are obtained from the area illustrated as the white line in the images.

from fitting of the data are plotted in Fig. 4(b) and (c), respectively. For all the measurements, the value  $n$  obtained from the fitting is close to 1. Thus, the CPE behaves close to an ideal capacitor. The oxide thickness is derived from the capacitance assuming the oxide acts as a parallel-plate capacitor with a dielectric constant  $\epsilon_r = 10$ . It should be said that values between 7.5 and 15 have been reported in the literature [3].

The  $R_p$  value of the AA 6063 alloy and especially the Al(1 1 1) are much higher than for the other samples. This indicates that these samples have a more compact and as a result a more protective oxide layer. For the AA 7075 alloy the  $Y_0$  value is higher and the  $R_p$  value is lower, which indicates a more defective open oxide. The determined oxide thicknesses are between 16 and 25 Å.

#### 3.4. Atomic force microscopy

For micro-structural information of the surface, AFM measurements of the surface on three different samples [Al(1 1 0), AA 6063 and AA 7075] were performed. The images are shown in Fig. 6. Below each image there is a line profile for the corresponding image above. The line profiles are obtained from the area inside the white rectangle and indicate the roughness of the surfaces. From the images and the line profiles it can be concluded that the roughness of the AA 7075 (RMS roughness: 8.4 Å) is higher than for both the Al(1 1 0) (RMS roughness: 2.7 Å) and the AA 6063 alloy (RMS roughness: 2.2 Å).

### 4. Discussion

Fig. 7 shows the oxide thicknesses on several samples determined using XRR, EIS and XPS. The figure includes thicknesses determined from more XRR measurements than presented in Figs. 1 and 2. This section is divided into three parts discussing how the methods, the type of sample and the history of the sample affect the determined oxide thickness on the samples.

#### 4.1. Methods

The results from the different methods shows that the oxide thicknesses determined using XRR and XPS are in good agreement. However, the oxide thicknesses determined using EIS are generally thinner. Also the trend (see dashed lines in Fig. 7), if comparing the oxide thicknesses for different types of samples, does not follow the trend from either XRR or XPS. The trend for the thicknesses determined using EIS would have agreed better if the oxide on the AA 7075 alloy was found to be thicker than on the other samples, but instead it is found by EIS to be the thinnest. Several reasons,

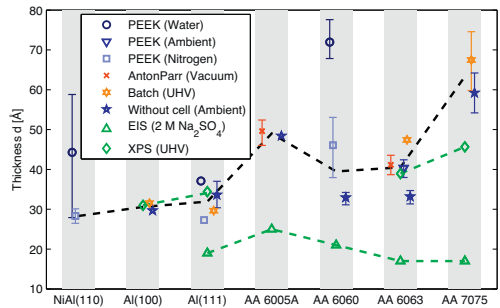


**Fig. 7.** Summary of the thicknesses achieved from the fitting of the XRR, EIS and XPS data. The dashed lines show the mean values of the XRR measurements in all environments except water, the EIS measurements, and the XPS measurements. The different data points for a sample are spread horizontally to increase readability. The error bars are shown for the XRR estimated thicknesses when the error are above 5%.

probably combined, could explain the discrepancy between the results from the EIS and the other methods.

An important reason is the value of the dielectric constant of the oxide in the parallel-plate capacitor model. The value characterizes the type of the oxide on the sample. In this report we have used a fixed value of  $\epsilon_r = 10$ . But in the literature values ranging from 7.5 to 15 have been reported [3], which is not surprising considering the many types of oxides that can be formed on Al. If a dielectric constant of around 15 are used instead, the thicknesses would be around 30 Å and agree better with the thicknesses determined using the other methods, except for the AA 7075 sample where it would still be a large discrepancy. There are possibilities that ionic species from the alloying elements effects the oxide and thereby the electric properties. In this context the AA 7075 alloy, which does not follow the trend, includes by far the highest content of alloying elements. Also, if comparing the Al 2p<sub>ox</sub> XPS peak of the different samples, the peak of AA 7075 in Fig. 3(d) is shifted to lower binding energy as compared to the Al 2p<sub>ox</sub> peaks from the other samples in Fig. 3(a)–(c). This indicates that this oxide is different from the oxides on the other samples.

Another possible reason arises from the difference between the model used in the EIS method and the actual oxide. The oxide in the model is a homogenous layer with the same thickness and same dielectric constant through the whole layer. This assumption is probably far from the actual structure of the oxide, which in many ways can be more heterogeneous, especially for the industrial alloys.

A possible heterogeneity could be local areas or spots where the oxide is thinner or have another structure/composition. These areas could act as electrical leakage sites during the EIS measurements, which result in a lower obtained oxide thickness. These local sites could be from where Al oxide islands coalesce during the oxide growth and/or from local dissolution especially in aqueous environments. For the industrial alloys there are more of these local sites as the alloying elements are known to form intermetallic phases present as micron-sized particles, nano-sized particles and dispersoids (50–60 nm). Oxides grown on these could be of another type and the particles or the boundary area surrounding the particles could be sites for higher dissolution compared to oxides grown on Al.

The results from the EIS and AFM indicate that the AA 7075 alloy is more heterogeneous than the other samples. The AFM images, show that the AA 7075 surface is rougher than the surface of other Al alloys with less alloying elements (AA 6063) and the single

crystal (Al(1 1 0)). The higher  $R_p$  and lower  $Y_0$  value for the AA 6063 and the Al(1 1 1) than for the AA 7075 indicate that the oxide of the latter includes heterogeneous structural defects such as cracks, dents, pits, fissures, etc. More leakage sites for the AA 7075 sample could explain the larger discrepancy between the results from the different methods for this sample.

The model used here to fit the EIS data is simplified and the reality is probably significantly more complex. Apart from the structural complexity as described above influencing the measured data, the actual measured interfacial capacitance originates not only from the oxide, but also from the double layer capacitance. For thick oxides, the measured capacitance is a good approximation of the oxide capacitance. However, for thin oxides, this approximation may induce considerable error in the calculated oxide thickness. Construction of an appropriate model (equivalent circuit) for a complete description of the EIS results for a complex oxide in an electrolyte as in the present investigation is beyond the scope of this report.

Different types of oxides and local thickness deviations could also explain why the thicknesses determined using XPS agrees well with the thicknesses determined using XRR for all the samples measured except for the AA 7075 sample. In the model used for the determinations of the oxide thickness with XPS, the oxide and the Al substrate were modeled as homogenous and the parameters describing the sample were the same for all samples. As discussed above, the larger shift of the Al  $2p_{ox}$  for the AA 7075 compared to the other samples indicates that this oxide is of a different type. Also the AFM images shows that the surface of the AA 7075 is rougher, indicating deviating local thicknesses, which for the XPS determinations will have a large impact due to the exponential dependence of the attenuation with respect to the inelastic mean free path. Due to the larger difference between the model and the actual oxide, it is possible that the error of the determined thickness with XPS is higher and the agreement with the thickness determined with XRR is worse for the AA 7075 sample compared to the other samples.

Another difference between the XPS and XRR methods is that in the case of XPS only Al contributes to the peaks and the thickness estimation. The error in the estimated thicknesses would then be larger for samples with more alloying elements as they are not measured in the XPS method.

Heterogeneous oxides and the fact that the oxides on the samples are of different types does not influence the XRR determination as much as for the other methods. In the fitting procedure of the XRR data possible heterogeneities and different types of oxides are taken into account in the fitting procedure as the parameters describing the oxide have more freedom. Since the XRR method is by far the most direct method to determine the thickness as almost no assumptions concerning the sample are needed, it is reasonable to assume that the oxide thicknesses determined from XRR and XPS (since it shows similar results) are more accurate than the thicknesses determined using EIS.

#### 4.2. Type of sample

The XRR and XPS results, if not including the results from measurements in water, show that the highest oxide thickness are observed for the AA 7075 alloy followed by the other industrial alloys. Possible reasons for why the industrial alloys have thicker oxides than the single crystals could be related to the difference between the structure of the single crystal metal surfaces and the alloy surfaces.

As opposed to a single crystal surface, the industrial alloy surfaces are polycrystalline in nature. Therefore, there are several different Al surfaces as well as boundary between grains on the surface of an Al alloy, and it would suggest the existence of more

nucleation sites for the Al oxide. This in turn would give rise to a less ordered and most likely a less dense oxide, since more domain boundaries would be created as the Al oxide islands coalesce. The present assumption is consistent with the observed thickness trends for different Al samples. Indeed, it is natural to assume an easier migration of ions/charge through a sparse oxide matrix, which results in a faster mass transfer rate and a greater oxide thickness.

Another reason for the observed oxide thickness trends could be the different concentration of the alloying elements and their content, which effect have been discussed previously in the literature [35,36]. The alloying elements have a different reactivity and could influence the oxide growth, which may promote formation of a thicker Al oxide. The higher content of alloying elements could therefore explain the thicker oxide on the AA 7075.

#### 4.3. History of the sample

The Al oxide thicknesses, calculated from the XRR measurements of the same sample in varied conditions (UHV, nitrogen, ambient) vary over a range of  $\pm 10$  Å. Since these conditions are supposed to be non-destructive for the oxide and that the errors for the XRR fits cannot explain the spread, the variation in oxide thickness must have another reason.

It is likely that the observed differences could arise due to different histories of the sample from the polishing to the time the measurements are performed. For example, in the case of single crystals, slightly different polishing conditions or different temperatures could change the oxide thickness. For the industrial alloys, another very likely reason for the different obtained thicknesses could be slightly different compositions and structures even for samples of the same type. These differences could originate from that the samples are cut from different places of an extrusion profile.

It should however be noted that when comparing samples in ambient and in water conditions, the increase in oxide thickness is only due to the presence of the water. Since the same sample is used for the measurement in both environments, the history of the samples cannot explain the difference. The conclusion must therefore be that the oxide thickness increases when in water. Incorporation of water or hydrogen into the oxide could possibly transform the oxide to a hydroxide, which could be thicker. Another explanation could be that the hydrogen affects the Mott potential, which leads to facilitate materials transport. It should be mentioned that, when the alloys samples are instead exposed in an electrolyte, localized dissolution due to micro-galvanic corrosion could instead lead to a reduced oxide thickness.

## 5. Conclusions

We have determined the oxide thickness on several single crystals [NiAl(1 1 0), Al(1 0 0) and Al(1 1 1)] and several industrial Al alloys [AA 6005A, AA 6060, AA 6063 and AA 7075] by using XRR, EIS and XPS. The oxide thicknesses obtained from XRR and XPS measurements show excellent agreement, but results from EIS show consistently thinner oxide films. The overall oxide thickness trends obtained from these groups of techniques (XPS and XRR vs. EIS) is also quite different. We conclude that both the XRR and XPS estimations are more accurate for these thin and flat oxides than the EIS as the XRR is by far the most direct method and that their results agree well.

Possible reasons for the discrepancy could be associated to the construction of an appropriate model (equivalent circuit) for the EIS method. Indeed, the ideal model has to take into account many factors, such as possibly varying value of the dielectric constant,

possibility for formation of different oxides types and structural heterogeneities in the oxide layer. Construction and justification of such a model is a difficult task.

We also observe that the oxides on the industrial alloys are thicker than the oxides on the single crystals. We suggest that the reason for this is twofold: Firstly, the oxide grown on the grainy structure of the alloy surface is sparser, which allows easier mass transport through the oxide layer and results in a greater limiting thickness. Secondly, it is the different alloying elements that influence the oxide growth, since they have different reactivity and tend to form different stable oxides compared to Al oxides.

It was also observed that placing the samples in water results in a thicker oxide, possible due to a transformation of the oxide to a hydroxide or facilitated material transport by the water.

Finally, this report illustrates that utilization of several complementary experimental techniques is crucial for investigation of amorphous oxide films properties with high accuracy and reliability.

### Acknowledgments

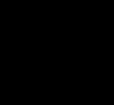
Parts of the experiments were performed on the ID03 beamline at the European Synchrotron Radiation Facility (ESRF), Grenoble, France, at the light source PETRA III at DESY, a member of the Helmholtz Association (HGF) and at the I311 beamline, MAX IV Laboratory, Lund, Sweden. We would like to thank O.H. Seck for assistance in using beamline P08. This work was financially supported by the Foundation for Strategic Research (SSF). The research leading to these results has received funding from the European Community's Seventh Framework Program (FP7/2007–2013) under grant agreement no. 312284.

### References

- [1] N. Cabrera, N.F. Mott, Theory of the oxidation of metals, Rep. Prog. Phys. 12 (1949) 163–184, <http://dx.doi.org/10.1088/0034-4885/12/1/308>
- [2] F.P. Fehlner, N.F. Mott, Low-temperature oxidation, Oxid. Met. 2 (1970) 59–99, <http://dx.doi.org/10.1007/BF00603582>
- [3] J.W. Schulz, M.M. Lohregel, Stability, reactivity and breakdown of passive films. Problems of recent and future research, Electrochim. Acta 45 (2000) 2499–2513, [http://dx.doi.org/10.1016/S0013-4686\(00\)00347-9](http://dx.doi.org/10.1016/S0013-4686(00)00347-9)
- [4] J.D. Baran, H. Grönbeck, A. Hellman, Mechanism for limiting thickness of thin oxide films on aluminum, Phys. Rev. Lett. 112 (2014) 146103, <http://dx.doi.org/10.1103/PhysRevLett.112.146103>
- [5] C.F. McConville, D.L. Seymour, D.P. Woodruff, S. Bao, Synchrotron radiation core level photoemission investigation of the initial stages of oxidation of Al(111), Surf. Sci. 188 (1987) 1–14, [http://dx.doi.org/10.1016/S0039-6028\(87\)80138-3](http://dx.doi.org/10.1016/S0039-6028(87)80138-3)
- [6] H. Brune, J. Wintterlin, R.J. Behm, G. Ertl, Surface migration of “hot” adatoms in the course of dissociative chemisorption of oxygen on Al(111), Phys. Rev. Lett. 68 (1992) 624–626, <http://dx.doi.org/10.1103/PhysRevLett.68.624>
- [7] C. Berg, S. Raen, A. Borg, J.N. Andersen, E. Lundgren, R. Nyholm, Observation of a low-binding-energy peak in the 2p core-level photoemission from oxidized Al(111), Phys. Rev. B 47 (1993) 13063, <http://dx.doi.org/10.1103/PhysRevB.47.13063>
- [8] L.P.H. Jeurgens, W.G. Sloof, F.D. Tichelaar, C.G. Borsboom, E.J. Mittemeijer, Determination of thickness and composition of aluminium-oxide overlayers on aluminium substrates, Appl. Surf. Sci. 144 (1999) 11–15, [http://dx.doi.org/10.1016/S0169-4332\(98\)00755-7](http://dx.doi.org/10.1016/S0169-4332(98)00755-7)
- [9] M. Schmid, G. Leonardelli, R. Tscheliessnig, A. Biedermann, P. Varga, Oxygen adsorption on Al(111): low transient mobility, Surf. Sci. 478 (2001) L355–L362, [http://dx.doi.org/10.1016/S0039-6028\(01\)00967-0](http://dx.doi.org/10.1016/S0039-6028(01)00967-0)
- [10] P.C. Snijders, L.P.H. Jeurgens, W.G. Sloof, Structure of thin aluminium-oxide films determined from valence band spectra measured using XPS, Surf. Sci. 496 (2002) 97–109, [http://dx.doi.org/10.1016/S0039-6028\(01\)01591-6](http://dx.doi.org/10.1016/S0039-6028(01)01591-6)
- [11] D. Starodub, T. Gustafsson, E. Garfunkel, The reaction of O<sub>2</sub> with Al(110): a medium energy ion scattering study of nano-scale oxidation, Surf. Sci. 552 (2004) 199–214, <http://dx.doi.org/10.1016/j.susc.2004.01.019>
- [12] N. Cai, G. Zhou, K. Müller, D.E. Starr, Tuning the limiting thickness of a thin oxide layer on Al(111) with oxygen gas pressure, Phys. Rev. Lett. 107 (2011) 035502, <http://dx.doi.org/10.1103/PhysRevLett.107.035502>
- [13] N. Cai, G. Zhou, K. Müller, D.E. Starr, Effect of oxygen gas pressure on the kinetics of alumina film growth during the oxidation of Al(111) at room temperature, Phys. Rev. B 84 (2011) 125445, <http://dx.doi.org/10.1103/PhysRevB.84.125445>
- [14] A. Hasnaoui, O. Politano, J.M. Salazar, G. Aral, Nanoscale oxide growth on Al single crystals at low temperatures: variable charge molecular dynamics simulations, Phys. Rev. B 73 (2006) 035427, <http://dx.doi.org/10.1103/PhysRevB.73.035427>
- [15] G. Kresse, M. Schmid, E. Napetschnig, M. Shishkin, Lukas Köhler, P. Varga, Structure of the ultrathin aluminum oxide film on NiAl(110), Science 308 (2005) 1440–1442, <http://dx.doi.org/10.1126/science.1107783>
- [16] M. Schmid, G. Kresse, A. Buchsbaum, E. Napetschnig, S. Gritschneider, M. Reichling, P. Varga, Nanotemplate with holes: ultrathin alumina on Ni<sub>3</sub>Al(111), Phys. Rev. Lett. 99 (2007) 196104, <http://dx.doi.org/10.1103/PhysRevLett.99.196104>
- [17] G. Prevot, S. Le Moal, R. Bernard, B. Crosset, R. Lazzari, D. Schmaus, Archetypal structure of ultrathin alumina films: grazing-incidence X-ray diffraction on Ni(111), Phys. Rev. B 85 (2012) 205450, <http://dx.doi.org/10.1103/PhysRevB.85.205450>
- [18] F. Mansfeld, M.W. Kendig, Evaluation of anodized aluminum surfaces with electrochemical impedance spectroscopy, J. Electrochem. Soc. 135 (1988) 828–833, <http://dx.doi.org/10.1149/1.2095786>
- [19] F. Bertram, F. Zhang, J. Evertsson, F. Carl, J. Pan, M.E. Messing, A. Mikkelsen, J.-O. Nilsson, E. Lundgren, In situ anodization of aluminum surfaces studied by X-ray reflectivity and electrochemical impedance spectroscopy, J. Appl. Phys. 116 (2014) 034902, <http://dx.doi.org/10.1063/1.4890318>
- [20] R. Essehli, B. El Bali, A. Faik, S. Benmohktar, B. Manouf, Y. Zhang, X.J. Zhang, Z. Zhou, H. Fuess, Structural changes upon lithium insertion in Ni<sub>0.5</sub>TiPO<sub>4</sub>, J. Alloys Compd. 530 (2012) 178–185, <http://dx.doi.org/10.1016/j.jallcom.2012.03.103>
- [21] F.U. Renner, A. Stierle, H. Dosch, D.M. Kolb, T.-L. Lee, J. Zegenhagen, Initial corrosion observed on the atomic scale, Nature 439 (2006) 707–710, <http://dx.doi.org/10.1038/nature04465>
- [22] The Aluminum Association, <http://www.aluminum.org/>
- [23] M.L. Foresti, A. Pozzi, M. Innocenti, G. Pezzatini, F. Loglio, E. Salvietti, A. Giusti, F. D'Anca, R. Felici, F. Borgatti, In situ X-ray analysis under controlled potential conditions: an innovative setup and its application to the investigation of ultrathin films electrodeposited on Ag(111), Electrochim. Acta 51 (2006) 5532–5539, <http://dx.doi.org/10.1016/j.electacta.2006.02.031>
- [24] P. Bernard, K. Peters, J. Alvarez, S. Ferrer, Ultrahigh vacuum/high pressure chamber for surface X-ray diffraction experiments, Rev. Sci. Instrum. 70 (1999) 1478–1480, <http://dx.doi.org/10.1063/1.1149609>
- [25] Anton Paar GmbH, DHS1100: a new high-temperature attachment for materials science in the whole orientation space, J. Appl. Cryst. 40 (2007) 202, <http://dx.doi.org/10.1107/S0021889806047224>
- [26] O.H. Seck, C. Deiter, K. Pflaum, F. Bertam, A. Beerlink, H. Franz, J. Horbach, H. Schulte-Schrepping, B.M. Murphy, M. Greve, O. Magnusson, The high-resolution diffraction beamline P08 at PETRA III, J. Synchrotron Rad. 19 (2012) 30–38, <http://dx.doi.org/10.1107/S0909049511047236>
- [27] S. Ferrer, F. Comin, Surface diffraction beamline at ESRF, Rev. Sci. Instrum. 66 (1995) 1674, <http://dx.doi.org/10.1063/1.1145879>
- [28] R. Nyholm, J.N. Andersen, U. Johansson, B.N. Jensen, I. Lindau, Beamline I311 at MAX-LAB: a VUV/soft X-ray undulator beamline for high resolution electron spectroscopy, Nucl. Instrum. Methods Phys. Res. A 520 (2001) 520–524, [http://dx.doi.org/10.1016/S0168-9002\(01\)00399-0](http://dx.doi.org/10.1016/S0168-9002(01)00399-0)
- [29] L.G. Parratt, Surface studies of solids by total reflection of X-rays, Phys. Rev. 95 (1954) 359–369, <http://dx.doi.org/10.1103/PhysRev.95.359>
- [30] L. Névoit, P. Croce, Caractérisation des surfaces par réflexion rasante de rayons X. Application à l'étude du polissage de quelques verres silicates, Rev. Phys. Appl. 15 (1980) 761–779, <http://dx.doi.org/10.1051/rphysap:01980001503076100>
- [31] M.R. Alexander, G.E. Thompson, X. Zhou, G. Beanson, N. Fairley, Quantification of oxide film thickness at the surface of aluminium using XPS, Surf. Interface Anal. 34 (2002) 485–489, <http://dx.doi.org/10.1002/sia.1344>
- [32] QUASES-Tougaard Inc., <http://www.quases.com/>
- [33] S. Tanuma, C.J. Powell, D.R. Penn, Calculations of electron inelastic mean free paths: V. Data for 14 organic compounds over the 50–2000 eV range, Surf. Interface Anal. 21 (1994) 165–176, <http://dx.doi.org/10.1002/sia.740210302>
- [34] M.E. Orazem, B. Tribollet, Electrochemical Impedance Spectroscopy, John Wiley & Sons, Inc., 2008, pp. 236, <http://dx.doi.org/10.1002/9780470381588>
- [35] C. Blanc, G. Mankowski, Susceptibility to pitting corrosion of 6056 aluminium alloy, Corros. Sci. 39 (1997) 949–959, [http://dx.doi.org/10.1016/S0010-938X\(97\)81160-2](http://dx.doi.org/10.1016/S0010-938X(97)81160-2)
- [36] J. Ryl, J. Wysocka, M. Jarzynka, A. Zielinski, J. Orlikowski, K. Darowicki, Effect of native air-formed oxidation on the corrosion behavior of AA 7075 aluminum alloys, Corros. Sci. 87 (2014) 150–155, <http://dx.doi.org/10.1016/j.corsci.2014.06.022>



Paper II





# Materials Research Express



## PAPER

### Surface development of an aluminum brazing sheet during heating studied by XPEEM and XPS

RECEIVED  
4 August 2016

REVISED  
5 October 2016

ACCEPTED FOR PUBLICATION  
7 October 2016

PUBLISHED  
27 October 2016

L Rullik<sup>2</sup>, F Bertram<sup>1</sup>, Y R Niu<sup>3</sup>, J Evertsson<sup>2</sup>, T Stenqvist<sup>4</sup>, A A Zakharov<sup>3</sup>, A Mikkelsen<sup>2</sup> and E Lundgren<sup>2</sup>

<sup>1</sup> DESY Photon Science, Notkestr. 85, D-22607 Hamburg, Germany

<sup>2</sup> Division of Synchrotron Radiation Research, Department of Physics, Lund University, Box 118, SE-221 00 Lund, Sweden

<sup>3</sup> MAX IV Laboratory, Lund University, Box 118, SE-221 00 Lund, Sweden

<sup>4</sup> Gränges Technology, SE-61281 Finspång, Sweden

E-mail: [lisa.rullik@sljus.lu.se](mailto:lisa.rullik@sljus.lu.se)

Keywords: brazing, aluminum alloy, XPEEM

#### Abstract

X-ray photoelectron emission microscopy (XPEEM) was used in combination with other microscopic and spectroscopic techniques to follow the surface development of an aluminum brazing sheet during heating. The studied aluminum alloy sheet is a composite material designed for vacuum brazing. Its surface is covered with a native aluminum oxide film. Changes in the chemical state of the alloying elements and the composition of the surface layer were detected during heating to the melting temperature. It was found that Mg segregates to the surface upon heating, and the measurements indicate the formation of magnesium aluminate. During the heating the aluminum oxide as well as the silicon is observed to disappear from the surface. Our measurements is in agreement with previous studies observing a break-up of the oxide and the outflow of the braze cladding onto the surface, a process assisted by the Mg segregation and reaction with surface oxygen. This study also demonstrates how XPEEM can be utilized to study complex industrial materials.

#### 1. Introduction

Aluminum alloys are found in a wide range of products because of their characteristic properties: low density, high strength, and good thermal conductivity and corrosion resistance. Due to their major industrial importance, aluminum products have been studied intensively. They can be found in diverse applications ranging from transport to construction industry. Thanks to their good thermal conductivity aluminum alloys are also used as heat exchangers in vehicles.

The assembly of aluminum work pieces into a heat exchanger is done by brazing. This is possible because the work pieces are formed out of composite alloys. The base aluminum alloy is covered by braze cladding that consists of an Al-Si filler alloy, see figure 1. The melting range of the braze cladding is lower than the one of the core material, thus the braze cladding can be molten selectively, flow between the work pieces, and form a joint upon cooling. On top of the braze cladding an aluminum oxide film forms spontaneously in an oxygen containing environment. This aluminum oxide layer obstructs the contact between the metal parts and needs to be removed up to create a firm joint. To achieve this, brazing is commonly performed in vacuum or in a protective environment at a temperature of 600 °C [1]. The discovery that Mg makes flux free brazing possible has facilitated vacuum brazing [2]. A vacuum better than  $<10^{-5}$  mbar is needed to prevent the reformation of the aluminum oxide.

A major research effort has been made in surface science to provide insight in the mechanisms of the initial oxidation of aluminum and the structure of the formed oxide [3–15]. We recently studied the thickness of native oxides on aluminum single crystals and aluminum alloys [16] as well as during *in situ* anodization [17].

Previously the decomposition of aluminum oxide in brazing alloys was examined using a hot stage scanning electron microscopy (SEM) [18]. It was shown that the aluminum oxide layer is broken up by exudations of

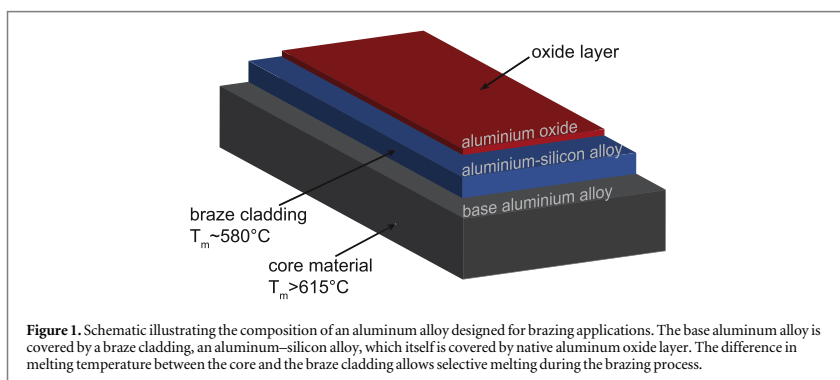


**Figure 1.** Schematic illustrating the composition of an aluminum alloy designed for brazing applications. The base aluminum alloy is covered by a brazing cladding, an aluminum–silicon alloy, which itself is covered by native aluminum oxide layer. The difference in melting temperature between the core and the brazing cladding allows selective melting during the brazing process.

**Table 1.** Chemical composition of the sample. Quantities given in wt% and [at%].

		Si	Fe	Cu	Mn	Mg	Ti	Bi	Al
Cladding	(FA7856)	9.7	0.22	—	—	0.67	—	0.08	Remainder
		[9.36]	[0.11]	—	—	[0.75]	—	[0.01]	Remainder
Core	(FA7825)	0.16	0.22	0.33	0.83	0.23	0.16	—	Remainder
		[0.15]	[0.11]	[0.14]	[0.41]	[0.26]	[0.09]	—	Remainder

molten material that burst up on the surface. Further, the difference between the thermal expansion coefficients of the thin aluminum oxide and the brazing cladding is suspected to play a part in the break-up [1].

In this paper we have studied *in situ* heat induced changes and final melting of a brazing cladding on a composite sheet for vacuum brazing in ultra high vacuum (UHV), using a combination of spectroscopic photoemission and low-energy electron microscopy (SPELEEM) [6, 19] and x-ray photoemission spectroscopy (XPS) complemented by *ex situ* SEM.

The advantage of SPELEEM is the chemical information on a microscopic scale, which is unobtainable with XPS and SEM. We were able to follow the decomposition of the native oxide film and the segregation of alloying elements upon melting. In addition to the insights into the changes upon heat treatment of an advanced aluminum alloy, this report illustrates how synchrotron radiation based SPELEEM can be utilized to study complex industrial materials. Its various modes of operation allow to characterize the sample's topography by low energy electron microscopy (LEEM), identify different elements in the surface layer in a microscopic selected areas with  $\mu$ -XPS and x-ray photoemission electron microscopy (XPEEM), which provides images with contrast due to the concentration of elements and their chemical states. To the authors knowledge, no other XPEEM-based studies on aluminum brazing sheets have been reported.

## 2. Experimental

The brazing alloy used was supplied by Gränges technology. It is a composite of the core material FA7825 with FA7856 brazing cladding on both sides. The total thickness was 0.40 mm and the thickness of the brazing cladding amounted about 50  $\mu$ m. The composition of the core material and the brazing cladding is shown in table 1. Further, the brazing cladding is covered by the native aluminum oxide film. Prior to the experiments all samples were cleaned successively with ethanol and acetone in an ultrasonic bath.

The *ex situ* characterization of the sample by SEM was done using a Hitachi SU8010 Cold Field Emission SEM at the Lund Nano Lab. To obtain images showing the topography of the sample's surface, secondary electrons were used.

Measurements with the SPELEEM were performed at the Swedish National Synchrotron Radiation facility, MAX IV laboratory, in Lund, using a SPELEEM [20] (Elmitec GmbH). The SPELEEM is situated at the undulator based soft x-ray beamline I311 [21], which provides photons in the energy range of 42.5–1500 eV. The energy resolution provided by the beamline is less than 100 meV. The SPELEEM is equipped with an energy analyzer which enables energy-filtered XPEEM. The general layout of the SPELEEM is described elsewhere [22]. The microscope has been moved to a new site at the 1.5 GeV ring at MAX IV laboratory. Due to the significant

inhomogeneity of the sample, our study uses a wide field of view (FOV), sacrificing some of the resolution of the instrument, but capturing a larger number of co-existing phases.

The temperature was measured using a thermocouple attached to the sample holder. This resulted in a measured temperature error of around 80 °C higher at a sample temperature of 500 °C. Therefore, in the presented experiments, we found that the sample melts at 500 °C instead of the known melting temperature of the braze cladding of 580 °C. A similar error was found when using a Minolta/LAND Cyclops 41 pyrometer due to the changing emissivity as the surface changes in composition with increasing temperature. We have therefore corrected all temperatures by adding 80 °C to the measured thermocouple value. The error of the temperature corrected in this way is estimated to be  $\pm 30$  °C, almost correct for the melting temperature and largest for the lower temperatures. The sample was heated to the respective temperatures and then held at that temperature for 15 min. Afterwards the sample was cooled to approximately 100 °C before imaging.

The experiments were performed in two separate experimental sessions. During the first experiment the measurements were performed after subsequent heating to 480 °C and 580 °C. The sample was found to melt at 580 °C, making any PEEM/LEEM measurements using high voltages impossible due to discharges. In the second session a new sample was used and smaller temperature steps were chosen. Data was acquired at 460 °C, 500 °C, 540 °C and 560 °C. The sample was heated further to 570 °C but partial melting occurred, again making further PEEM/LEEM measurements impossible.

The XPS spectra were extracted from the images of the dispersive plane, where one image provides a 15 eV wide energy window of the analyzer. The Al 2p, Mg 2p and Si 2p spectra were recorded using a photon energy of 133 eV while the photon energy for the O 1s spectra was 580 eV. The sampling area for the spectra was 9  $\mu\text{m}$ . Linear backgrounds have been subtracted from all spectra. Peak positions were determined by fitting Doniach–Sunjić lineshape to the data [23]. XPEEM images for Al 2p, Mg 2p, Si 2p and LEEM images were recorded using a photon energy of 133 eV and a FOV of 50  $\mu\text{m}$ .

### 3. Results

#### 3.1. Spectroscopy

In this section we describe the development of the surface composition of the braze cladding using XPS from a probing area of 10  $\mu\text{m}$  as the temperature is increased in steps until melting occurs.

##### 3.1.1. Aluminium

In figure 2(a) the evolution of the Al 2p spectra during heating is shown. The spectrum recorded after the sample was heated to 460 °C is shown on the bottom of figure 2(a). Two components were fitted to the data corresponding to one component at BE = 76.5 eV which we attribute to aluminum oxide ( $\text{Al}_2\text{O}_3$ ) shown in gray and one component assigned to magnesium aluminate ( $\text{MgAl}_2\text{O}_4$ ) shown in dark blue at BE = 76.0 eV [24, 25]. The assignment may not be obvious since the oxide peak is broad, however the  $\text{MgAl}_2\text{O}_4$  has been observed previously in similar brazing materials [26] by auger electron spectroscopy. By heating the sample from 460 °C to 480 °C the total signal increases, which we attribute to the desorption of adsorbed hydrocarbons on the surface since the ratio between aluminum oxide and magnesium aluminate stays nearly constant.

Heating further to 500 °C we find that the amount of magnesium aluminate increases slightly while the contribution of the aluminum oxide decreases. At 540 °C the peak shifts towards lower binding energies and the emission is mainly from the  $\text{MgAl}_2\text{O}_4$  at 76.0 eV and various other compounds with lower binding energies. Further, emission from metallic Al 2p starts to appear at lower binding energies.

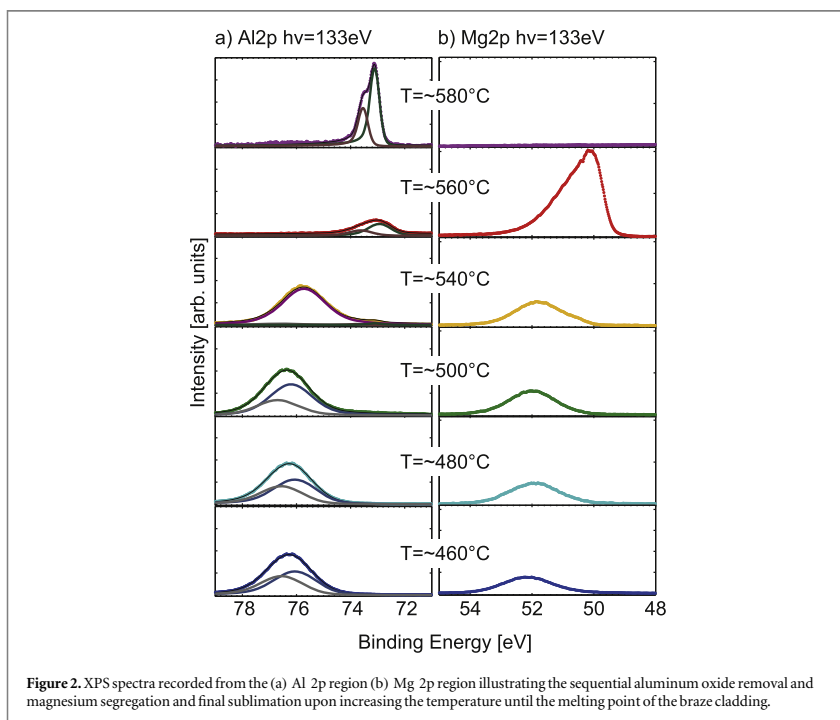
At 560 °C no signal is observed in the aluminum oxide binding energy range, but only a relatively weak metallic aluminum peak can be detected. The total intensity of aluminum has decreased significantly. The increase of the Mg 2p signal at the same temperature indicates that a magnesium rich layer is covering the surface.

By heating to 580 °C a steep increase in the intensity of the metallic peak occurs, suggesting that the metallic aluminum is not covered by any other material. The two fitted components correspond to Al  $2p_{1/2}$  and Al  $2p_{3/2}$  with a spin–orbit split of 0.43 eV close to the reported value [5].

##### 3.1.2. Magnesium

A better understanding of the behavior of the Al 2p level in figure 2(a) upon melting can be gained by studying the Mg 2p level when performing the same heating experiment. In figure 2(b) the corresponding changes in the magnesium spectrum upon heating are shown.

In figure 2(b) Mg 2p spectra are shown at temperatures from 460 °C to 580 °C. At 460 °C the binding energy of a single component fitted to the data has a peak position at a binding energy of 52.1 eV. With increasing temperature the peak shifts to lower binding energies. At a temperature of 540 °C the binding energy has shifted



to 51.8 eV and a small amount of metallic magnesium at 49.8 eV can be detected. After heating to 560 °C a strong signal for metallic magnesium appears at a binding energy of around 49.8 eV and the signal for magnesium oxide is reduced but is likely to continue to contribute to the emission at higher binding energies as a broad shoulder. In general, the broad appearance of the Mg 2p emission indicates a mixture of magnesium compounds at the surface. By heating the sample further to 580 °C no peak in the Mg 2p line could be detected, suggesting the sublimation of Mg into vacuum or diffusion into the bulk.

The development of Al and Mg is graphically summarized in figure 3. It shows that the native oxide disappears as the braze cladding is melting in conjunction with the segregation and sublimation of Mg.

### 3.1.3. Oxygen

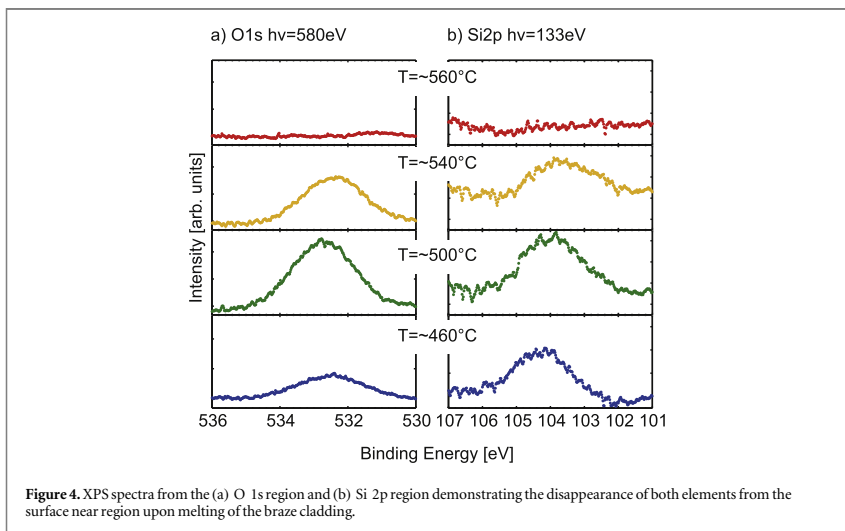
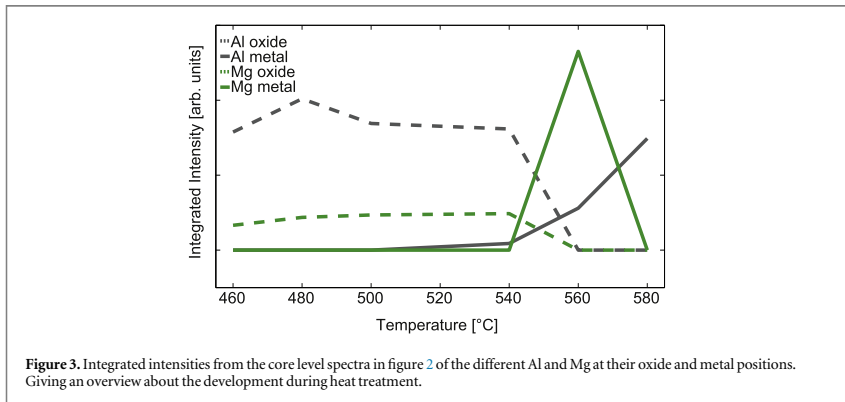
In figure 4(a) XPS spectra from the O 1s region are shown as the temperature is increased. At 460 °C a broad O 1s emission line can be detected, indicating a contribution from oxygen atoms in several different surroundings, such as pure aluminum oxide, the magnesium aluminate structure and other aluminum magnesium and silicon oxides.

As the temperature is increased to 500 °C, the overall intensity is increasing indicating the desorption of adsorbates from the surface, in agreement with the observations for the Al 2p and Mg 2p levels. At 540 °C the O 1s signal is decreasing slightly, and a shift towards lower binding energy is observed, which could be due to the formation of a more  $MgAl_2O_4$  like structure as observed in the Al 2p and Mg 2p levels. At 560 °C no O 1s emission can be detected, demonstrating the disappearance of the oxide.

The disappearing of the oxygen signal at 560 °C agrees well with the oxide disappearance in the XPS spectra from the Al 2p and Mg 2p regions in figures 2(a) and (b), respectively.

### 3.1.4. Silicon

Turning to the Si 2p core level region shown in figure 4(b), only emission at around 104 eV can be detected at 460 °C. During the further heating the peak shifts slightly to lower binding energies which indicates that the present oxidized silicon species becomes slightly reduced. Clearly, the assignment of this emission is not straightforward and could be due to several Si containing compounds.



However, no pure Si could be detected at a binding energy of 99.6 eV. A similar trend as for the oxygen signal as a function of the temperature is also observed for the silicon core level region. By heating to 500 °C the intensity of the signal increases, and by heating to 540 °C it decreases again. At 560 °C, the Si 2p emission is no longer observable. The signal intensity of the silicon XPS spectra is significantly lower than that for magnesium after normalization. This indicates that even though the absolute concentration of silicon in the braze cladding is higher than the one of magnesium, less silicon is present in the surface near region.

### 3.2. Microscopy

In this section we report on the microscopic investigations by LEEM and XPEEM recorded in conjunction with the XPS measurements described above.

#### 3.2.1. LEEM/MEM

The images shown in figures 5(a) and (b) were obtained in an intermediate LEEM and MEM mode. In LEEM a coherent low energy electron beam is impinging on the sample's surface. To obtain bright field images as shown here, the specular beam of diffracted electrons is selected [27–29]. By using a very low start voltage electrons that have been reflected at the equipotential surface just slightly above the actual surface contributed to the contrast in the presented images.

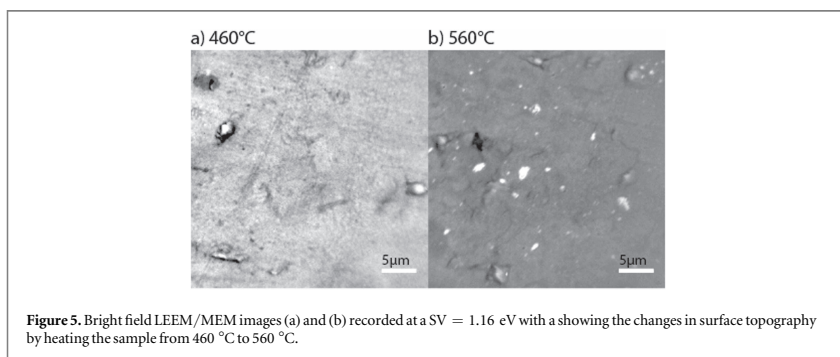


**Figure 5.** Bright field LEEM/MEM images (a) and (b) recorded at a  $SV = 1.16$  eV with a showing the changes in surface topography by heating the sample from 460 °C to 560 °C.

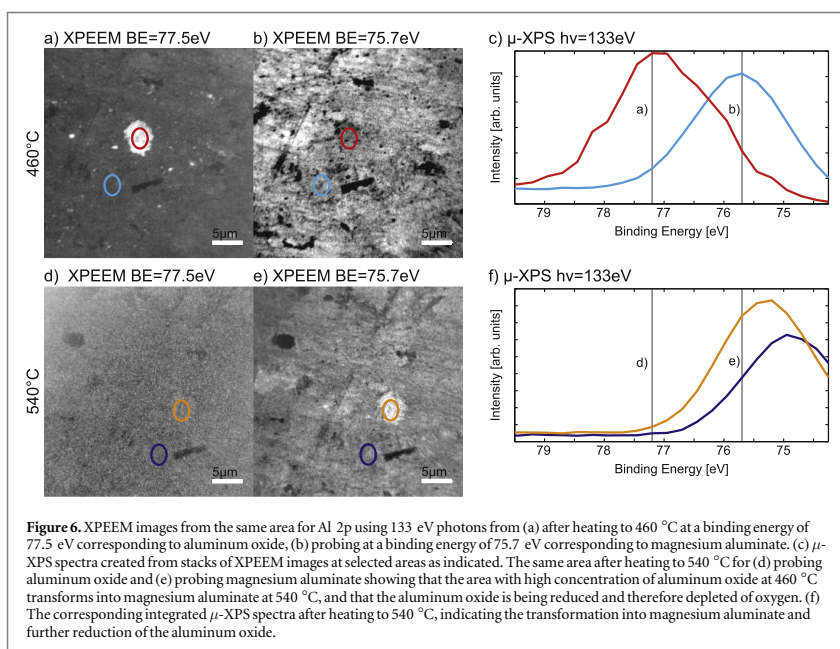


**Figure 6.** XPEEM images from the same area for Al 2p using 133 eV photons from (a) after heating to 460 °C at a binding energy of 77.5 eV corresponding to aluminum oxide, (b) probing at a binding energy of 75.7 eV corresponding to magnesium aluminate. (c)  $\mu$ -XPS spectra created from stacks of XPEEM images at selected areas as indicated. The same area after heating to 540 °C for (d) probing aluminum oxide and (e) probing magnesium aluminate showing that the area with high concentration of aluminum oxide at 460 °C transforms into magnesium aluminate at 540 °C, and that the aluminum oxide is being reduced and therefore depleted of oxygen. (f) The corresponding integrated  $\mu$ -XPS spectra after heating to 540 °C, indicating the transformation into magnesium aluminate and further reduction of the aluminum oxide.

In figures 5(a) and (b) the changes in the surface topography upon heating are visualized by the LEEM/ME; images. The image in figure 5(a) recorded after heating to 460 °C shows that the surface appears flat and homogeneous. By heating the sample to 560 °C, bright spots appears in the image, as can be seen in figure 5(b). Recalling that at this temperature, Mg segregates to the surface, see figure 2(b), the bright spots are likely to consist of Mg, which will be supported by the XPEEM observations described below.

### 3.2.2. XPEEM Aluminum

In this section, energy-filtered core level images, so called XPEEM images are presented. The contrast in the images is related to the corresponding core-level photoelectron yield. This means that areas shown bright in the XPEEM image correspond to a higher concentration of the elements at that particular binding energy.

In figure 6(a) one can identify brighter particles on top of a darker background. Since the image was obtained after heating to 460 °C at a binding energy of 77.5 eV assigned to aluminum oxide, the bright spots indicate the presence of aluminum oxide.

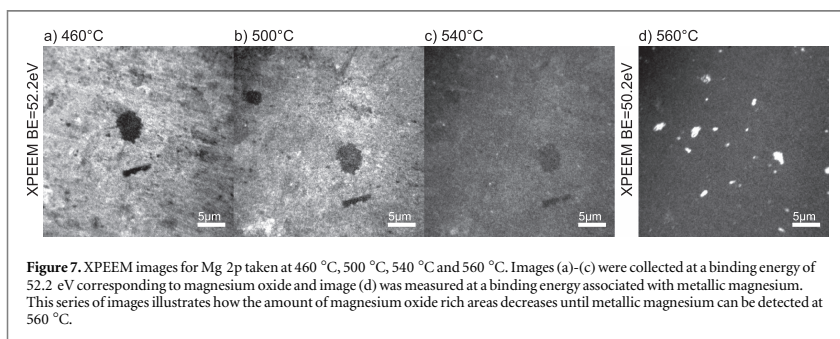


**Figure 7.** XPEEM images for Mg 2p taken at 460 °C, 500 °C, 540 °C and 560 °C. Images (a)–(c) were collected at a binding energy of 52.2 eV corresponding to magnesium oxide and image (d) was measured at a binding energy associated with metallic magnesium. This series of images illustrates how the amount of magnesium oxide rich areas decreases until metallic magnesium can be detected at 560 °C.

At the same temperature, the bright appearance of the XPEEM image recorded at a binding energy of 75.7 eV indicates the simultaneous presence of a magnesium aluminate-like phase as shown in figure 6(b), recorded at lower binding energies. Interestingly, the large spot (marked in red) appears dark at this energy and annealing temperature, indicating a low concentration of magnesium aluminate in this particular area.

By heating the sample to 540 °C the bright spot (marked in orange) appears at a binding energy of 75.7 eV, which can be related to magnesium aluminate, as shown in figure 6(e). From the  $\mu$ -XPS of the red/orange marked area, the transformation of an aluminum oxide rich particle into a magnesium aluminate-rich particle can be observed by the shift in binding energy. The areas marked in light/dark blue also shift slightly to lower binding energies. This indicates that aluminum is reduced during the heat treatment. The  $\mu$ -XPS spectra, figures 6(c) and (f), were created from the integrated intensities of the selected areas in XPEEM stacks. The two exemplary areas that are presented in figure 6 are comparable to the two components fitted to the XPS spectra shown in figure 2(a).

### 3.2.3. XPEEM Magnesium

In figures 7(a), (b) and (c) XPEEM images recorded at an energy of 52.2 eV corresponding to an oxidized species of magnesium. XPEEM images for the Mg 2p region after heating to 460 °C, 500 °C and 540 °C are shown, respectively. The larger spot as discussed in the Al 2p XPEEM images appear to be depleted in magnesium oxide content in comparison with the surrounding surface.

The contrast between the larger spot and the surrounding surface is decreasing with increasing temperature. This shows that the distribution of oxidized magnesium becomes more even while the overall intensity of the signal at 52.2 eV decreases. This is in agreement with the shift to lower binding energies observed in the XPS spectra shown in figure 2(b).

Turning to the XPEEM image corresponding to the emission from metallic Mg, figure 7(d), we observe the amount of Mg on the surface increases significantly all over the surface, and in particular at some micron sized areas on the surface. The diameter of these particles ranges approximately from 0.2 to 1.7  $\mu\text{m}$ . The segregation of magnesium particles to the surface at 560 °C is in accordance with the strong increase in the metallic magnesium signal in the XPS spectrum in figure 2(b).

### 3.2.4. XPEEM Silicon

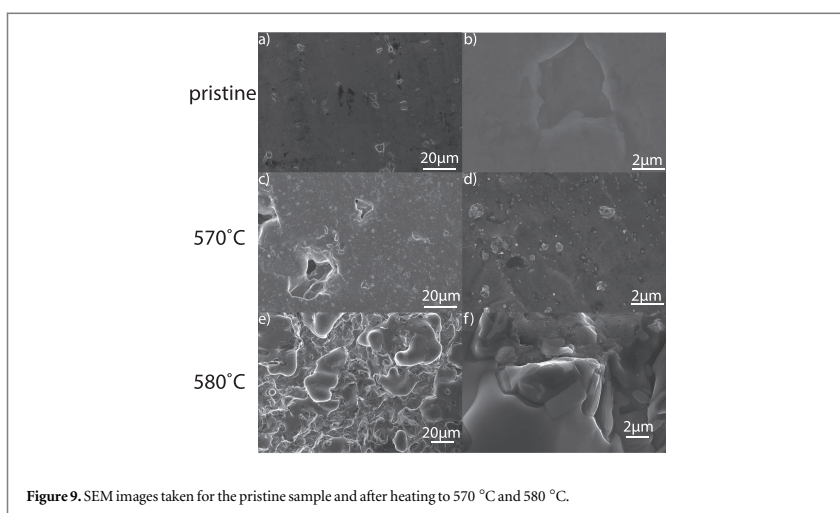
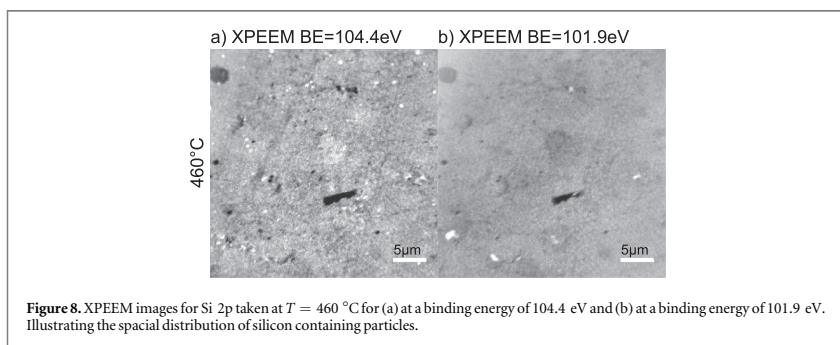
In figure 8(a) the same feature near the center is bright as in figure 6(a) as well as a number of smaller bright features at the surface. These particular areas have therefore a high concentration of silicon oxide. However the signal is surprisingly low, considering the amount of Si present in the braze cladding. The largest of these particles are 0.2  $\mu\text{m}$ . A few minor features appear bright at a binding energy of 101.9 eV.

### 3.2.5. SEM Results

We now turn to SEM images recorded *ex situ* after the heating within the SPELEEM. The temperatures for the *ex situ* SEM measurements were slightly higher as compared to the temperatures used in the SPELEEM measurements, due to the trial-and-error in attempting to avoid arching effects in the SPELEEM instrument.

Figure 9(a) displays a large area SEM images of the pristine surface. The surface appears relatively homogeneous apart from some defects at the surface. Figure 9(b) shows a zoom-in of the surface.

After heating to 560 °C a partly melted surface can be observed as evidenced by the appearance of larger holes in figure 9(c). In addition, smaller particles can be observed at the surface figure 9(d) which presumably is due to



the remaining Mg on the surface, since the size of the particles is close to the Mg particle size observed in the SPELEEM measurements.

Finally, after heating to 580 °C the surface is observed to be almost completely melted 9(e), however some parts of the surface appears to be smoother than other parts, see figure 9(f). The difference in roughness of the different areas shows the inhomogeneity of the melted and reoxidized sample surface.

#### 4. Discussion

Until 460 °C the surface consists mainly of aluminum oxide, magnesium aluminate and magnesium oxide with small areas of silicon oxide. At this temperature the braze cladding is still completely covered with a relatively flat oxide film. In general, it is challenging to distinguish between the different compounds present in the top layer because of the complexity of the sample and the technical assignment of the exact binding energies. First of all, the large number of different oxidized aluminum compounds that can form due to the different alloying element makes an unambiguous assignment difficult. Furthermore, as a result of several different compounds in the surface near region, the XPS core levels will appear broad. An additional contribution to the uncertainty in the assignment of the core level components is that the XPS spectra were acquired by a single image of the dispersive plane. Therefore, the assigned binding energy can be slightly deviating from the actual binding energy.

Keeping all these factors in mind we can return to the alloy at 460 °C. Looking at the XPEEM images, we may identify a central spot, which is bright in figure 6(a), and figure 8(a) but dark in figure 7. This indicates that the

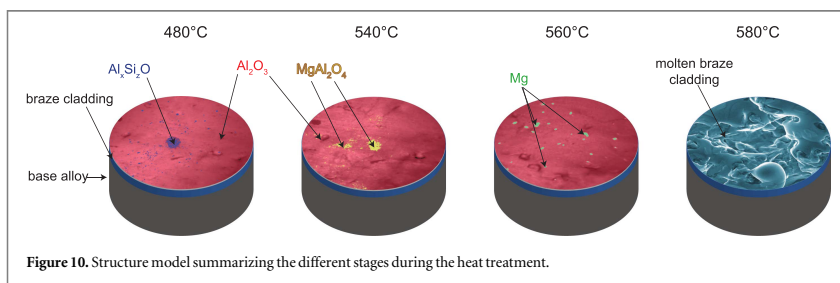


Figure 10. Structure model summarizing the different stages during the heat treatment.

area is rich in aluminum oxide and silicon oxide but depleted in magnesium oxide. There are also several similar but smaller spots spread over the surface. These are shown in blue in the structure model shown in figure 10.

Apart from the particles being rich in both aluminum and silicon oxides, there are also a number of particles that consist of pure silicon oxide, as can be seen in figure 8(a). This is in agreement with the rather broad silicon peak in figure 4(b). Considering the previously discussed methodological challenges the peak can nevertheless be assigned to silicon oxide [30] but the presence of magnesium silicide can not be excluded.

Spread all over the surface are aluminum oxide and magnesium aluminate. Occasionally these species occur in distinct areas as illustrated in figure 6. These two components were also fitted to the XPS spectrum shown in figure 2(a). The peaks are at slightly higher binding energies than expected from the literature [24, 25, 31] and it is not possible to exclude that other compounds with a similar binding energy as aluminum oxide and magnesium aluminate might be present.

Magnesium can be observed in the oxide layer as magnesium oxide and magnesium aluminate. Here the binding energy of 52.1 eV matches previously reported values of 52.2 eV for magnesium oxide [32].

By increasing the heat further to 540 °C slight shifts in the XPS spectra of aluminum, magnesium, figure 2, and silicon, figure 4(b), towards lower binding energies can be observed. The 2D representation of the shift is also found in the XPEEM images of Al and Mg, see figures 6 and 7. The previously described aluminum and silicon oxide rich spot, shown in blue in the model in figure 10, is changing from a more aluminum oxide rich into a magnesium aluminate rich area.

To understand how this area changes upon heating we have to consider the high diffusivity of magnesium in aluminum at elevated temperatures [33]. In figure 3 we can see that the integrated intensity of magnesium oxide increases during the heating. This suggests that the heating of the alloy results in magnesium diffusing towards the surface and reacts with the oxide present in the surface near layers. Due to magnesium having a low electron negativity and high affinity to oxygen, it may react with the oxygen in an oxide such as for example silicon oxide, which is present in small areas all over the surface. Possible reactions for the formation of magnesium oxide are shown in the following.



The reduced silicon may then diffuse into the bulk of the alloy as has previously been observed [34]. An indication for the reduction of the silicon oxide as the magnesium is segregating is found in the XPS spectra shown in figure 4(b), where at 540 °C the peak broadens towards lower binding energies.

After the magnesium has formed a magnesium oxide, it can react further with aluminum oxide to form the magnesium aluminate.



Other possible reaction pathway is the direct formation of magnesium aluminate from magnesium and aluminum or aluminum oxide.



The magnesium aluminate formation has been studied previously and supports the present observations [35, 36]. Heating the alloy further to 560 °C we can observe in figure 3 how the intensities for all oxides disappears completely. This is in accordance with the XPS signal for oxygen, which disappears at the same temperature as demonstrated in figure 4(a). Metallic magnesium is appearing at the surface and is predominant

on the surface since the metallic aluminum signal is low. The magnesium peak in the XPS spectrum shown in figure 2(b) for 560 °C is most intense at the expected metallic peak position of 49.8 eV, but tails off at the higher binding energies. This shows that different compounds of oxidized magnesium (or possibly other compounds) are still present and contribute to the broad peak.

By continuing to heat the sample, magnesium disappears from the surface and pure metallic aluminum dominates the surface layer.

## 5. Conclusion

Throughout the heat treatment of the aluminum alloy in UHV, we were able to follow the decomposition of the oxide layer covering the braze cladding. Our study indicates the pure  $\text{Al}_2\text{O}_3$ ,  $\text{MgAl}_2\text{O}_4$  as well as mixed Al and Si oxides are present at the surface up to 460 °C. As the temperature is increased, Mg starts to segregate, leading to an increase of the amount of  $\text{MgAl}_2\text{O}_4$  and a simultaneous reduction of Si which diffuses into the bulk.

Upon further increase of the temperature the XPS signals for oxygen, aluminum oxide, magnesium oxide and silicon oxide disappear and emission corresponding to metallic aluminum and magnesium is observed. The present observations are in good agreement with previous studies observing a break-up of the oxide and the outflow of the braze cladding onto the surface due to differences in thermal expansion between the aluminum oxide and the braze/core material [1].

Using XPEEM, mixed Al and Si oxide-rich particles could be observed, as well as identification of the formation of  $\text{MgAl}_2\text{O}_4$  areas at intermediate temperatures. The segregation and formation micrometer large magnesium-rich particles at the surface was observed at 560 °C. At 570 °C partial melting of the surface layer was discovered. Subsequent heating of the sample to 580 °C lead to the disappearance of the metallic magnesium peak in the XPS spectrum and a further increase in intensity of the metallic aluminum signal. The surface layer was molten at 580 °C but areas of the magnesium rich non-molten surface were indicated by *ex situ* SEM.

## Acknowledgments

This work was financially supported by the Swedish Foundation for Strategic Research (SSF project RMA11-0090, Aluminum oxides for processing and products (ALUX)).

## References

- [1] Lentz A H, Dickerson P B, Robinson I B and Saunders H L 1990 *Aluminum Brazing Handbook* (Washington, DC: Aluminum Association)
- [2] Miller C J 1967 Aluminum brazing US Patent no. US3321828
- [3] McConville C, Seymour D, Woodruff D and Bao S 1987 *Surf. Sci.* **188** 1
- [4] Brune H, Wintterlin J, Behm R J and Ertl G 1992 *Phys. Rev. Lett.* **68** 624
- [5] Berg C, Raen S, Borg A, Andersen J N, Lundgren E and Nyholm R 1993 *Phys. Rev. B* **47** 13063
- [6] Schmidt T, Heun S, Slezak J, Diaz J, Prince K C, Lilienkamp G and Bauer E 1998 *Surf. Rev. Lett.* **05** 1287
- [7] Jeurgens L, Sloof W, Tichelaar F, Borsboom C and Mittemeijer E 1999 *Appl. Surf. Sci.* **144** 145 11
- [8] Snijders P, Jeurgens L and Sloof W 2002 *Surf. Sci.* **496** 97
- [9] Starodub D, Gustafsson T and Garfunkel E 2004 *Surf. Sci.* **552** 199
- [10] Kresse G, Schmid M, Napetschnig E, Shishkin M, Köhler L and Varga P 2005 *Science* **308** 1440
- [11] Schmid M, Kresse G, Buchsbaum A, Napetschnig E, Gritschneider S, Reichling M and Varga P 2007 *Phys. Rev. Lett.* **99** 196104
- [12] Cai N, Zhou G, Müller K and Starr D E 2011 *Phys. Rev. Lett.* **107** 035502
- [13] Cai N, Zhou G, Müller K and Starr D E 2011 *Phys. Rev. B* **84** 125445
- [14] Zähr J, Oswald S, Türpe M, Ullrich H and Füssel U 2012 *Vacuum 5th Int. Symposium on Vacuumbased Science and Technology SVST5 86* (Kaiserslautern, Germany 28th-30th September 2010) 1216
- [15] Baran J D, Grönbeck H and Hellman A 2014 *Phys. Rev. Lett.* **112** 146103
- [16] Evertsson J *et al* 2015 *Appl. Surf. Sci.* **349** 826
- [17] Bertram F, Zhang F, Evertsson J, Carl F, Pan J, Messing M E, Mikkelsen A, Nilsson J-O and Lundgren E 2014 *J. Appl. Phys.* **116** 034902
- [18] McGurran B and Nicholas M 1984 *J. Mater. Sci.* **19** 2713
- [19] Locatelli A, Aballe L, Mentès T O, Kiskinova M and Bauer E 2006 *Surf. Interface Anal.* **38** 1554
- [20] Zakharov A, Mikkelsen A and Andersen J 2012 *J. Electron Spectrosc. Relat. Phenom.* **185** 417
- [21] Nyholm R, Andersen J, Johansson U, Jensen B and Lindau I 2001 *Nucl. Instrum. Methods Phys. Res. A* **467-468** 520
- [22] Locatelli A, Mentès T O, Nino M A and Bauer E 2011 *Ultramicroscopy* **111** 1447
- [23] Doniach S and Šunjić M 1970 *J. Phys. C: Solid State Phys.* **3** 285
- [24] Lindsay J R, Rose H J, Swartz W E, Watts P H and Rayburn K A *Appl. Spectrosc.* **27** 1
- [25] Mattogno G, Righini G, Montesperelli G and Traversa E 1993 *Appl. Surf. Sci.* **70** 1 363
- [26] Swaney O W, Trace D E and Winterbottom W L 1986 *Weld. J.* **65** 49
- [27] Bauer E 1994 *Rep. Prog. Phys.* **895**
- [28] Bauer E 1998 *Surf. Rev. Lett.* **05** 1275
- [29] Tromp R 2000 *IBM J. Res. Dev.* **44** 503
- [30] Qi B, Olafsson S, Zakharov A, Göthelid M, Agnarsson B and Gislason H 2013 *Appl. Surf. Sci.* **264** 349

- [31] Olefjord I, Stenqvist T and Karlsson A 1994 Surface oxide of braze clad aluminium *Tech. Rep. T presented at the 4th Int. Conf. on Aluminum Alloys Atlanta, Georgia, Sep. 11-16, 1994*, Gränges Technology Centre 94/908
- [32] Mizuno K, Nylund A and Olefjord I 1996 *Mater. Sci. Technol.* **12** 306
- [33] Funamizu Y and Watanabe K 1972 *Trans. Japan Inst. Met.* **13** 278
- [34] Lacaze J, Tierce S, Lafont M-C, Thebault Y, Pbre N, Mankowski G, Blanc C, Robidou H, Vaumousse D and Daloz D 2005 *Mater. Sci. Eng. A* **413414** 317 *Int. Conf. on Advances in Solidification Processes*
- [35] McLeod A D and Gabryel C M 1992 *Metall. Trans. A* **23** 1279
- [36] Kim K 2015 *Surf. Interface Anal.* **47** 429

NUNC EST BIBENDUM